



Evaluating China's anthropogenic CO₂ emissions inventories: a northern China case study using continuous surface observations from 2005 to 2009

Archana Dayalu^{1,a}, J. William Munger^{2,3}, Yuxuan Wang^{4,5}, Steven C. Wofsy^{2,3}, Yu Zhao⁶, Thomas Nehrkorn¹, Chris Nielsen³, Michael B. McElroy³, and Rachel Chang⁷

¹Atmospheric and Environmental Research, Lexington, MA, USA

²Earth and Planetary Sciences, Harvard University, Cambridge, MA, USA

³School of Engineering and Applied Sciences, Harvard University, Cambridge, MA, USA

⁴Department of Earth and Atmospheric Sciences, University of Houston, Houston, TX, USA

⁵Department of Earth System Sciences, Tsinghua University, Beijing, China

⁶School of the Environment, Nanjing University, Nanjing, China

⁷Department of Physics and Atmospheric Science, Dalhousie University, Halifax, Canada

^aformerly at: Earth and Planetary Sciences, Harvard University, Cambridge, MA, USA

Correspondence: Archana Dayalu (adayalu@aer.com)

Received: 25 July 2019 – Discussion started: 12 September 2019

Revised: 14 February 2020 – Accepted: 26 February 2020 – Published: 25 March 2020

Abstract. China has pledged reduction of carbon dioxide (CO₂) emissions per unit of gross domestic product (GDP) by 60 %–65 % relative to 2005 levels, and to peak carbon emissions overall by 2030. However, the lack of observational data and disagreement among the many available inventories makes it difficult for China to track progress toward these goals and evaluate the efficacy of control measures. To demonstrate the value of atmospheric observations for constraining CO₂ inventories we track the ability of CO₂ concentrations predicted from three different CO₂ inventories to match a unique multi-year continuous record of atmospheric CO₂. Our analysis time window includes the key commitment period for the Paris Agreement (2005) and the Beijing Olympics (2008). One inventory is China-specific and two are spatial subsets of global inventories. The inventories differ in spatial resolution, basis in national or subnational statistics, and reliance on global or China-specific emission factors. We use a unique set of historical atmospheric observations from 2005 to 2009 to evaluate the three CO₂ emissions inventories within China's heavily industrialized and populated northern region accounting for ~33 %–41 % of national emissions. Each anthropogenic inventory is combined with estimates of biogenic CO₂ within a high-resolution atmospheric transport framework to model the time series of

CO₂ observations. To convert the model–observation mismatch from mixing ratio to mass emission rates we distribute it over a region encompassing 90 % of the total surface influence in seasonal (annual) averaged back-trajectory footprints (L_{0.90} region). The L_{0.90} region roughly corresponds to northern China. Except for the peak growing season, where assessment of anthropogenic emissions is entangled with the strong vegetation signal, we find the China-specific inventory based on subnational data and domestic field studies agrees significantly better with observations than the global inventories at all timescales. Averaged over the study time period, the unscaled China-specific inventory reports substantially larger annual emissions for northern China (30 %) and China as a whole (20 %) than the two unscaled global inventories. Our results, exploiting a robust time series of continuous observations, lend support to the rates and geographic distribution in the China-specific inventory. Though even long-term observations at a single site reveal differences among inventories, exploring inventory discrepancy over all of China requires a denser observational network in future efforts to measure and verify CO₂ emissions for China both regionally and nationally. We find that carbon intensity in the northern China region has decreased by 47 % from 2005 to 2009, from approximately 4 kg of CO₂ per USD (note that

all references to USD in this paper refer to USD adjusted for purchasing power parity, PPP) in 2005 to about 2 kg of CO₂ per USD in 2009 (Fig. 9c). However, the corresponding 18 % increase in absolute emissions over the same time period affirms a critical point that carbon intensity targets in emerging economies can be at odds with making real climate progress. Our results provide an important quantification of model–observation mismatch, supporting the increased use and development of China-specific inventories in tracking China's progress as a whole towards reducing emissions. We emphasize that this work presents a methodology for extending the analysis to other inventories and is intended to be a comparison of a subset of anthropogenic CO₂ emissions rates from inventories that were readily available at the time this research began. For this study's analysis time period, there was not enough spatially distinct observational data to conduct an optimization of the inventories. The primary intent of the comparisons presented here is not to judge specific inventories, but to demonstrate that even a single site with a long record of high-time-resolution observations can identify major differences among inventories that manifest as biases in the model–data comparison. This study provides a baseline analysis for evaluating emissions from a small but important region within China, as well a guide for determining optimal locations for future ground-based measurement sites.

1 Introduction

China's contribution to world CO₂ emissions has been steadily growing, becoming the largest in the world in 2006. China has accounted for 60 % of the overall growth in global CO₂ emissions over the past 15 years (US EIA, 2017). Under the United Nations Framework Convention on Climate Change (UNFCCC) 2015 Paris Agreement, China has committed to reducing its carbon intensity (CO₂ emissions per unit of gross domestic product, GDP) by 60 %–65 % relative to the baseline year of 2005, and to peak carbon emissions overall by or before 2030. Demonstration of progress on emissions reduction and evaluation of how well specific policies are working is hindered by large uncertainty in the existing Chinese emission inventories. In 2012 the discrepancy between data reported at national and provincial levels was approximately half of China's 2020 emission reduction goals (US EIA, 2017; NDRC, 2015; Guan et al., 2012; Zhao et al., 2012). Moreover, China is under mounting pressure to address severe regional air pollution events that are often associated with CO₂ emissions sources – vehicles, power plants, and other fossil-fuel-burning operations. China's 11th Five Year Plan (11th FYP) of 2006–2010 included aggressive measures to retire inefficient coal-fired power plants and improve energy efficiency in other industries starting in 2007 (Zhao et al., 2013; Nielsen and Ho, 2013). A number of pollution control measures that were implemented specifically

in preparation for the 2008 Beijing Summer Olympics were also largely in effect by the end of 2007 (Nielsen and Ho, 2013; Wang et al., 2010).

A variety of top-down approaches including inverse analysis (Le Quéré et al., 2016) and comparison between atmospheric observations and Eulerian forward model predictions (X. Wang et al., 2013) have been used to evaluate and constrain emission estimates, albeit at coarse spatial resolution. As noted by Wang et al. (2011) grid-based atmospheric models have difficulty in simulating high-concentration pollution plumes at specific receptor sites that are too near the source region. The expanding network of high-accuracy CO₂ observations coupled with high spatial resolution transport models is emerging as a viable tool for evaluating high-resolution emission inventories (e.g., Sargent et al., 2018). In this paper we adopt a Lagrangian transport model to simulate atmospheric mixing and transport. Continuous observations of CO₂ for the period 2005–2009 at Miyun, an atmospheric observatory about 100 km northeast of Beijing, provide a top-down constraint for evaluating persistent bias among emissions rates obtained from a suite of three independent anthropogenic emission inventories that were readily available as spatially gridded fluxes.

The three inventories that are evaluated span a range of bottom-up inventory approaches. They are not intended to be an exhaustive set, but are examples to demonstrate the capability to identify significant differences in the ability of different inventories to match the long time series of observations. Emerging inventory approaches based on updated (yet non-China-specific) point-source data and satellite observations of night lights as a proxy for spatial allocation of energy production (Oda et al., 2018) were not readily available when this analysis began. Two of the inventories, the Emissions Database for Global Atmospheric Research (EDGAR; European Commission, Joint Research Centre/Netherlands Environmental Assessment Agency, 2013) and Carbon Dioxide Information Analysis Center (CDIAC), are spatial subsets from larger global models of CO₂ emissions (European Commission, Joint Research Centre/Netherlands Environmental Assessment Agency, 2013; Andres et al., 2016a). They rely on national-level energy statistics and global default values for sectoral emission factors, and they estimate activity levels using generalized proxies (e.g., population). The third inventory (ZHAO) is specific to China, with greater reliance on energy statistics at provincial and individual facility levels as well as emission factors from domestic field studies (Zhao et al., 2012). The ZHAO inventory was readily accessible at the time of this research and represents increased efforts in recent years to incorporate more China-specific data into emissions inventories. Other China-specific inventories that have been recently developed but were not readily available at the time of this research include the Multi-resolution Emissions Inventory (MEIC, <http://www.meicmodel.org/>, last access: 12 April 2019) and an inventory by Shan et al., 2016. The primary intent of the

comparisons presented here is not to judge specific inventories, but to demonstrate that even a single site with a long record of high-time-resolution observations can identify the potential impact of major differences among inventories that manifest as biases in the model–data comparison.

A study by Turnbull et al. (2011) used weekly flask observations to evaluate a hybrid approach to inventory construction where CDIAC and EDGAR estimates were spatially allocated to a provincial emissions-based grid. However, to our knowledge, none of the truly China-specific CO₂ inventories have been evaluated with independent high-temporal-resolution atmospheric observations. The official national total for China's 2005 CO₂ emissions from energy-related activities, used as the benchmark for the Paris commitment, is approximately 5.4 Gt CO₂ (NDRC, 2015). ZHAO, EDGAR, and the CDIAC national total (Boden et al., 2016) report total 2005 energy-related CO₂ emissions that are higher by 31 % (7.1 Gt), 9 % (5.9 Gt), and 7 % (5.8 Gt), respectively. As the official national total is not available in a spatially allocated format, it cannot be tested by observations and we refer to it only as a benchmark in our analysis. We will show that the China-specific inventory (ZHAO) provides excellent agreement with observations, and markedly more so than EDGAR and CDIAC. The result provides guidance for efforts to assess China's emissions at larger scales as well as potential updates for the Paris Agreement base-year emissions.

In order to independently evaluate and scale existing bottom-up estimates of China's CO₂ emissions, we employ a top-down approach using 5 years of continuous CO₂ observations. Modeled concentrations of CO₂ are obtained from convolving hourly CO₂ surface flux estimates with surface influence estimates (“footprints”) derived from the Stochastic Time-Inverted Lagrangian Transport Model driven with meteorology from the Weather Research and Forecasting Model version 3.6.1 (WRF-STILT; Lin et al., 2003; Nehrkorn et al., 2010). NOAA CarbonTracker (CT2015) provides modeled estimates of advected upwind background concentrations of CO₂ that are enhanced or depleted by processes in the study region. As atmospheric CO₂ concentrations are significantly modulated by photosynthetic and respiratory fluxes, we additionally prescribe hourly biosphere fluxes of CO₂ using data-driven outputs from the Vegetation, Photosynthesis, and Respiration Model (VPRM) adapted for China (Mahadevan et al., 2008; Dayalu et al., 2018a). VPRM provides a functional representation of biosphere fluxes based on data from remote sensing platforms and eddy flux towers, with significantly better observationally validated performance relative to subsets of global vegetation models (Dayalu et al., 2018a). The WRF-STILT-VPRM framework has been successfully adapted for similar emissions evaluation studies in North America in regions where biogenic fluxes dominate surface processes (e.g., Sargent et al., 2018; Karion et al., 2016; Matross et al., 2006). For the northern China region, anthropogenic fluxes exceed biogenic fluxes for all but the peak of growing season, when they are roughly com-

parable (Dayalu et al., 2018a), which reduces the magnitude of overall error from incorrect modeling of the biosphere. In contrast to extensive measurement networks that exist in North America, continuous high-temporal-resolution measurements of CO₂ necessary for inventory evaluation applications are sparse and very few datasets are available in China (Wang et al., 2010). Despite this limitation, our site provides valuable information and constraints on emissions inventories: the long time series and spatial sampling heterogeneities, where the site receives both clean continental air as well as air from one of the heaviest emitting regions of China, present a powerful and unique dataset for the region. Our inventory scaling is confined to the northern China region, but this region accounts for 33 %–41 % of China's total annual CO₂ emissions from fossil-fuel combustion. Model–observation mismatches can be converted from concentration units (ppm) to mass units (Mt CO₂) across the most relevant area subset from modeled annual average surface sensitivity footprints (ppm CO₂ μmol⁻¹ CO₂ m² s). Ultimately, we compare the inventories by quantifying model–observation mismatch for seasons (using additive mass units) and annually (using scaling factors). We note that identical transport fields and modeled biogenic fluxes are applied to all the anthropogenic emission fields. Unresolved transport error and error in biogenic fluxes undoubtedly contributes to scatter in the model–data comparison. While random transport errors are unlikely to generate consistent biases among the inventories, systematic transport errors can be attributed to biases among inventories with differing spatial allocations. Although the interaction of systematic transport errors with differences in spatial distribution could bias individual observations, averaging over longer timescales (seasons, years) minimizes the bias of individual points. With the available observational data it is not possible to evaluate the error in spatial allocation of individual emissions inventories. For example, future access to total column measurements and/or aircraft vertical profiles would provide additional constraints on spatial allocations of sources and sinks.

Section 2 of this paper describes the observational CO₂ record used in this analysis. Section 3 details the analysis methods, including WRF-STILT model configuration, a discussion of the main features of the inventories, error evaluation, and inventory scaling methods. We present the results in Sect. 4, beginning with an assessment of seasonality impacts. We then compare inventory performance against observations across multiple timescales from hourly to annual. We conclude Sect. 4 with scaling results, and a brief examination of regional carbon intensity over the study period. Concluding remarks are provided in Sect. 5. Additional methodological details are provided in the accompanying Supplement and at <https://doi.org/10.7910/DVN/OJES00>.

2 CO₂ observations

This study uses 5 years (2005–2009) of continuous hourly averaged CO₂ observations (LI-COR Biosciences Li-7000; 2σ analytical precision of 0.08 ppm), measured at a site in northern China (Miyun; 40°29′ N, 116°46.45′ E). The Miyun receptor is an atmospheric measurement station in a rural site 100 km northeast of the Beijing urban center (Fig. S2 in the Supplement). It was established in 2004 by collaborating researchers at the Harvard China Project and operated by researchers at Tsinghua University. The site is strategically located to capture both clean continental background air from the west and northwest and polluted air from the Beijing region to the southwest. Miyun is located south of the foothills of the Yan mountains; the region consists of grasslands, small-scale agriculture intermingled with rural villages and manufacturing complexes, and mixed temperate forest. Land use varies from rural to suburban and dense urban to the south towards Beijing center and sparsely populated and wooded mountains to the north and west. Further descriptions of the site and details of the instrumentation including calibration strategy and assessment of long-term drifts are provided in Wang et al. (2010). Average annual data coverage (based on hourly data) over the study time period was 83 % (range: 78 % to 92 %).

3 Methods

We evaluate the performance of the ZHAO, EDGAR, and CDIAC inventories coupled with biogenic fluxes by modeling 5 years of hourly CO₂ observations using the Stochastic Time-Inverted Lagrangian Transport Model (STILT; Lin et al., 2003) run in backward time mode driven by high-resolution meteorology from the Weather Research and Forecasting Model version 3.6.1 (WRF). The WRF-STILT tool models the surfaces that influenced each measurement hour in the study domain (Fig. 1). Hourly vegetation CO₂ fluxes are prescribed by the VPRM adapted for China (Mahadevan et al., 2008; Dayalu et al., 2018a). We categorize seasons by months based on regional growing season patterns, which are heavily dominated by winter wheat and corn dual-cropping regions in the North China Plain (Dayalu et al., 2018a). Winter wheat emergence in the spring and corn emergence in later summer shift the seasonal patterns such that regional seasons are more appropriately represented as January, February, March (JFM, winter); April, May, June (AMJ, spring); July, August, September (JAS, summer); and October, November, December (OND, fall).

Ultimately, modeled concentrations of CO₂ are obtained from convolving hourly surface flux estimates with footprints derived from the WRF-STILT framework. NOAA CarbonTracker (CT2015) provides estimates of advected upwind background concentrations of CO₂ that are enhanced or depleted by processes in the study region. Our final model–

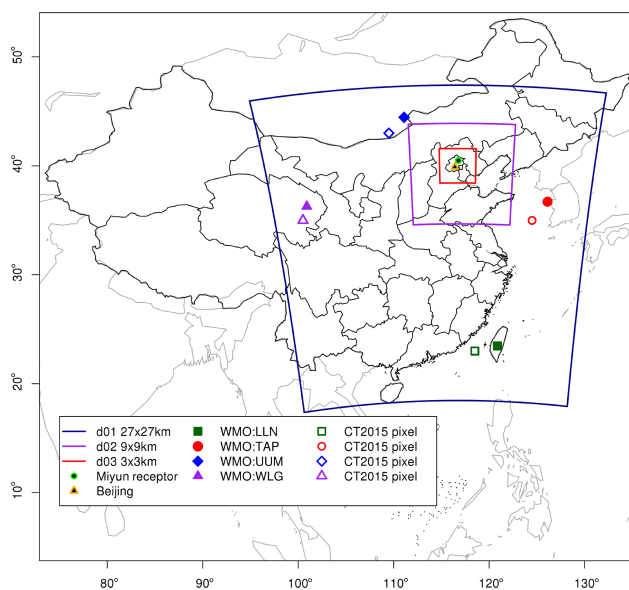


Figure 1. Study domain configuration. Miyun receptor and Beijing center are located within the innermost domain at a resolution of 3 × 3 km. NOAA ESRL/WMO (WMO) flask sampling sites used to evaluate bias in CT2015 modeled backgrounds are the solid shapes; nearest CT2015 comparison pixel is the corresponding unfilled shape.

measurement dataset is the subset consisting of local daytime values (hourly data from 11:00 to 16:00 LT). Of this subset, only individual hours for which observational data exist (i.e., non-missing data) are included. The final dataset was further filtered to include only CT2015 background values satisfying true background criteria as described in Sect. 3.4 and in Sect. S4 in the Supplement. As is typical for studies of this nature, our analysis focuses on observations during the 11:00 to 16:00 LT period. The stronger vertical mixing in the daytime atmosphere (notably absent at night) reduces the influence of extremely local emissions. We select the 11:00–16:00 window to avoid the presence of shallow inversion layers that are poorly represented in STILT and use the period when vertical mixing through the entire boundary layer is at its maximum (McKain et al., 2015; Sargent et al., 2018). We adjust fluxes based on model–measurement mismatch of this final data subset, focusing on the region that our model finds to be the most influential to the signal measured at the receptor. Method details and model components are described individually below.

3.1 WRF-STILT model configuration

The WRF-STILT particle transport framework and optimal configuration have been extensively tested in several studies using midlatitude receptors (e.g., Sargent et al., 2018; McKain et al., 2015; Kort et al., 2013; McKain et al., 2012; Miller et al., 2012). WRF is configured with 41 ver-

tical levels and two-way nesting in three domains, with the outermost domain covering nearly seven administrative regions (Figs. 1 and 2), defined according to convention in Piao et al. (2009). The domain resolutions from coarsest to finest are 27 km (d01), 9 km (d02), and 3 km (d03). Initial and lateral WRF boundary conditions are provided by NCEP FNL Operational Model Global Tropospheric Analyses at 1° × 1° spatial 6-hourly temporal resolution (NCEP, 1999). Nudging of fields is implemented in the outer domain only, and never within the planetary boundary layer (PBL). WRF output is evaluated against publicly accessible 24-hourly averaged observational datasets from the Chinese Meteorological Administration (CMA); finer temporal resolution meteorological data are not publicly available. WRF run details are presented in Dayalu (2017) and at <https://doi.org/10.7910/DVN/OJES00>. A snapshot of results from comparison with China Meteorological Administration ground-station measurements is presented Sect. S1 and Figs. S1–S4 in the Supplement.

The STILT model is configured in backward time mode. The particle release point is set as the Miyun measurement sample inlet (the receptor). The inlet height is 158 m a.s.l., corresponding to 6 m a.g.l. In our study, the hilltop site was located in an area where the surrounding land was not very productive or intensively cultivated (Fig. S2). There is a long history of using short towers in low-productivity areas for regional studies (e.g., NOAA Earth Systems Research Laboratory – NOAA ESRL Barrow, Alaska, observatory at 11 m a.g.l.). In addition, the station is located on a small hilltop, so even though the actual inlet height above ground is low, it has a topographic advantage in that it effectively samples air from a greater height relative to the surroundings. Topographic advantage was exploited in a similar manner in Karion et al. (2016) in the context of an Alaskan CO₂ study. However, Karion et al. (2016) were able to use a suite of additional data to confirm the validity of their assumption including comparisons to concurrent aircraft measurements and multiple inlets at 31.7, 17.1, and 4.9 m a.g.l. In our study, independent verification from concurrent aircraft measurements (for example) or multi-level inlet locations were not available to quantify the impact of absolute and relative inlet location on transport uncertainty.

Each hourly footprint (CO₂ concentration attributed to each unit of flux as ppm μmol⁻¹ m² s) provides an estimate of surface influence on the measurement and is calculated from releasing 500 particles from the measurement site (receptor) until they reach the outer domain boundaries up to 7 d back in time. The STILT 0.25° × 0.25° footprint map for each measurement hour up to 7 d back in time enables assessment of regions in the study domain to which the receptor is most sensitive. These entire gridded footprints are convolved with anthropogenic and biogenic CO₂ flux estimates to provide a final modeled concentration (ppm) of CO₂ at the receptor. For clarity, we display the regions of importance to the receptor based on contours calculated from the

overall STILT footprints at the 50th (L_{0.50} region), 75th (L_{0.75} region), and 90th (L_{0.90} region) percentile levels (Fig. 2). The percentile contours are calculated as follows: the average (seasonal, annual) footprints from 2005 to 2009 are ordered from high to low. We multiply each fraction (0.5, 0.75, 0.9) with the summed footprints and use cumulative sums of the ordered footprints as a guide to select all points with influence magnitude equal to or greater than this cut-off value. Figure S11 illustrates a single footprint map along with the average influence and a plot of cumulative influence to demonstrate the percentile-level selection process. We emphasize that we use the entire STILT footprint convolved with fluxes to estimate the receptor CO₂ concentration. We only use the L_{0.90} region to provide a reasonable area across which to ascribe the effective inventory adjustment (converted from parts per million model–observation mismatch to mass units). As Fig. S11c shows, the L_{0.90} region strikes a balance between capturing sufficient influence while avoiding an unrealistically large adjustment region for a single observation site. Conversely, corrections based on the smaller L_{0.75} region would include larger uncertainties from the diffuse influence of emissions outside the L_{0.75} region (not accounting for 25 % of average surface sensitivity), yet the model–observation mismatch would be ascribed to a region approximately half the area of the L_{0.90} region. Deriving correction factors based on integration over the entire L_{0.90} region is a more conservative approach where the model–observation mismatch in mass units is distributed over a larger area.

Further model details are available in Sect. S2. Complete WRF-STILT settings and STILT footprint files are available from <https://doi.org/10.7910/DVN/OJES00>.

3.2 Anthropogenic CO₂ emissions inventories

ZHAO, EDGAR, and CDIAC report estimates of total annual emissions of CO₂ at 0.25° × 0.25°, 0.1° × 0.1°, and 1° × 1° original grid resolutions, respectively. We regridded the EDGAR and CDIAC inventories to the 0.25° × 0.25° resolution, using the NCAR Command Language version 6.2.1 Earth System Modeling Framework “conserve” regridding algorithm to preserve the integral of emissions (Brown et al., 2012). Differences between annual total emissions for EDGAR and CDIAC inventories introduced by regridding are smaller than the interannual trends or differences between the inventories (Sect. S3 and Fig. S5). We present the main components and defining features of the three anthropogenic CO₂ inventories below.

The ZHAO inventory provides estimates of total annual emissions for 2005 through 2009. In addition, the spatial location of emissions is given for years 2005 and 2009 on a 0.25° × 0.25° grid. Using 2005 and 2009 gridded values, we calculate an average percent contribution of each grid cell to the total emissions. The average contributions are used as weights to spatially allocate 2006, 2007, and 2008 total an-

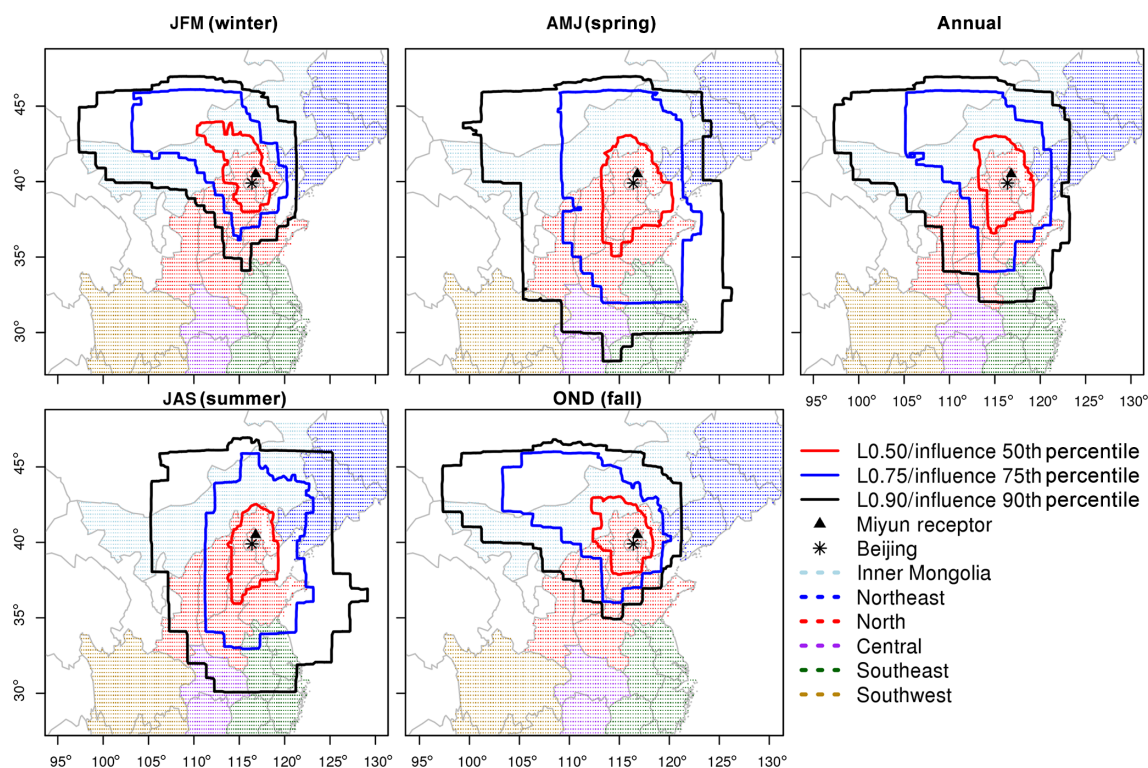


Figure 2. 2005–2009 mean seasonal (a–d) and Annual (e) footprint contours, as percentiles of influence highlighted by administrative region. Red, blue, and black contour lines represent 50th, 75th, and 90th percentile regions, respectively. Stippling represents location of $0.25^\circ \times 0.25^\circ$ footprint and inventory grid cell centers, colored by relevant administrative regions. Northern China (red stippling) is the administrative region with predominant influence on Miyun observations, followed by Inner Mongolia and northeastern China. Southeastern and central China have minimal representation, and only during the spring and summer seasons

nual emissions. We evaluate and justify this assumption in detail in Sect. S3 and Fig. S6. The ZHAO inventory represents one of the first statistically rigorous bottom-up CO₂ inventories for China. It relies on provincial- and facility-level data rather than national-level data, which has been noted previously as a major uncertainty in Chinese emission inventories; total CO₂ emissions estimates based on provincial data are typically higher than those using national statistics (Zhao et al., 2013). Satellite observations of criteria air pollutants (e.g., nitrogen dioxide, which serves as a proxy for fossil fuel combustion) show greater agreement with provincial statistics (Zhao et al., 2012). The increased use of China-specific emission factors and activity levels based on domestic field studies is a shift from other inventories that rely heavily on global averages to estimate processes occurring in China. Despite the increased incorporation of China-specific field data, the largest sources of uncertainty to the ZHAO inventory are industrial emission factors, and activity levels across all sectors. Total uncertainty in the inventory is estimated as -9% to $+11\%$ (Zhao et al., 2012).

The EDGAR emissions database continues to be a major prior in atmospheric studies, and the CO₂ inventory is used to inform key global scientific results considered by the UNFCCC Conference of Parties. The EDGAR global

inventory (atemporal EDGAR v4.2 FT2010 gridded emissions) takes total annual estimates of national emissions and downscales emissions to a $0.1^\circ \times 0.1^\circ$ as a function of road and shipping networks, population density, energy and manufacturing point sources, and agricultural land. Estimates for China are available for all 5 years as gridded inventories. Reported uncertainties for global emissions are $\pm 10\%$ (<https://themasites.pbl.nl/tridion/en/themasites/edgar/documentation/uncertainties/index-2.html>, last access: 10 February 2020). However, this applies to global averaged uncertainty; we expect uncertainty for China to be much higher.

We include the CDIAC inventory here due to its historical prevalence as a benchmark inventory for global indicators, including evaluations of carbon intensity provided by the World Bank (World Bank, 2017). The CDIAC inventory (v2016; <https://doi.org/10.3334/CDIAC/ffe.ndp058.2016>) allocates estimates of national emissions to a $1^\circ \times 1^\circ$ grid, primarily distributed according to human population density. A thorough assessment of 2σ uncertainties in the CDIAC spatial allocation of emissions shows considerable spread in regional uncertainties (Andres et al., 2016).

Our study is not intended to be an exhaustive sampling of inventory approaches but serves to demonstrate the util-

ity of continuous high-accuracy observations as a top-down constraint on emissions evaluations. Our inventory list notably does not include emerging spatially resolved global inventories (e.g., Open Data Inventory for Anthropogenic Carbon Dioxide, ODIAC) (Oda et al., 2018) that were not readily available at the time this work was conducted. At 1×1 km, ODIAC does have a high spatial resolution of night-light proxy-based emissions; while this is a valuable method for regions in Europe and North America for example, it is less valuable for China where it is analogous to the CDIAC population-based proxy. In China, power plant emissions are typically located far from end-use regions and the night-light proxy can often break down (R. Wang et al., 2013). Furthermore, ODIAC power plant emissions use the 2012 Carbon Monitoring for Action (CARMA) database, which notably does not incorporate China-specific power plant data; in these instances, CARMA categorizes China's power plants as "non-disclosed plants" and reports using estimates derived from statistical models using averaged emissions factors – comparable to methods in global inventories subset over China (Ummel, 2012). One of our main goals is to quantify model–observation mismatch associated with use of China-specific power plant data, and ODIAC does not address that issue particularly differently from other global emissions inventories subset over China. For completeness, however, evaluation of global inventories like ODIAC and a suite of increasingly available China-specific inventories (e.g., MEIC) would provide value as part of future model–observation comparison efforts.

Based on multi-year means (2005 to 2009) and 95 % confidence intervals derived from two-sample *t* tests, we find that within the L_{0.90} evaluation region EDGAR and CDIAC report emissions that are significantly lower than ZHAO by typically 20 % (−24 %, −16 %) and 36 % (−37 %, −34 %), respectively. Across China's administrative regions, the highest discrepancy between the global and regional inventories is in northern China (ZHAO is approximately 30 % higher than both EDGAR and CDIAC). In addition, northern China represents one of the administrative regions with the highest CO₂ emissions density (2300 to 3300 MgCO₂ km^{−2}, compared to the average of 700 MgCO₂ km^{−2} averaged across China) and is therefore a particularly rich spatial subset for emissions inventory evaluation. A detailed breakdown of emissions by region of China is provided in Table S1 in the Supplement. Spatial differences are displayed in Fig. S7.

Previous work has found that temporal variations in CO₂ sources can be significant and surface CO₂ can be perturbed by between 1.5 and 8 ppm within source regions based on the time of day and/or day of week, resulting from a combination of changes in activity patterns as well as synoptic-scale transport effects (Nassar et al., 2013). However, appropriate data for establishing reasonable temporal scaling factors for data-sparse regions such as China are difficult to obtain, and as in the case of Nassar et al. (2013) China's activity factors are based on US activity factors weighted according to China's

EDGARv4.2 emissions patterns. We applied the weekly and diurnal Nassar et al. (2013) scaling factors to our emissions, but these did not generate statistically significant differences from the unscaled versions. These statistically insignificant results suggest that a more rigorous set of temporal scaling factors need to be developed for China. CDIAC does provide monthly gridded inventories with seasonality embedded. However, predictions based on that seasonality deviated even further from the observations than predictions based on constant annual emissions. In the CDIAC global dataset, the seasonality in emissions is based upon generalized global activity factors that are not necessarily appropriate for estimating seasonality of human activity in China. Therefore, in this study we do not explicitly consider diel and seasonal variation in anthropogenic CO₂ fluxes.

3.3 Vegetation flux inventory

We prescribe biotic contributions to the CO₂ signal by adapting the VPRM model output for the study domain to generate $0.25^\circ \times 0.25^\circ$ gridded estimates of hourly CO₂ net ecosystem exchange (NEE) from 2005 to 2009. Details of the VPRM model and output for China are presented in Dayalu et al. (2018a). The VPRM is driven by 8 d 500 m MODIS surface reflectance values and 10 min averages of WRF downward shortwave radiation and surface temperature fields. The VPRM parameters are calibrated using eddy flux measurements in the study domain representing each ecosystem type classified according to the International Geosphere-Biosphere Programme (IGBP) scheme. Calibration and evaluation eddy-flux data are obtained from FluxNet and ChinaFlux collaborators. The L_{0.90} region is dominated by croplands (Fig. S8), in particular the winter wheat and corn dual cropping that characterizes the North China Plain (Dayalu et al., 2018a). We use one biosphere model in this study to simplify our assessment of variations across the different emissions inventories. Our selection of the VPRM in particular is based on results from Dayalu et al. (2018a), where the VPRM was shown to have significantly lower regional bias than an ensemble of global 3-hourly flux products subset over China.

3.4 Background concentrations

Appropriate quantification of background CO₂ concentrations (i.e., the CO₂ concentration at the lateral edges of the model domain and/or prior to interaction with domain surface processes) enables realistic assessment of the study domain's contribution to atmospheric CO₂ at varying timescales. CT2015 estimates of CO₂ concentrations are provided on a $3^\circ \times 2^\circ$ grid at upwind background locations. Background values are selected and corrected for large-scale biases using methodology similar to Karion et al. (2016) where a particle must originate from the outermost domain edge and/or 3000 m a.s.l.; further details are provided in

Sect. S4. The predicted background CO₂ is shown in Fig. 3a together with observed CO₂ at Miyun for the 11:00–16:00 LT period over the 5-year observational record. For most of the year the measured CO₂ shows large enhancements above background and only in midsummer is there a small depletion relative to background values.

3.5 Quantifying regional changes to background CO₂ concentrations: ΔCO₂

We define hourly ΔCO₂ as a regional change (enhancement or depletion) imparted to concentrations of CO₂ advected from the boundary (CO_{2,CT2015}) such that, for each observation hour ΔCO_{2,obs},

$$\Delta\text{CO}_{2,\text{obs}} = \text{CO}_{2,\text{obs}} - \text{CO}_{2,\text{CT2015}}. \quad (1)$$

For each modeled hour ΔCO_{2,mod}, *i* and *j* represent the surface grid cell locations and *h* represents the hour of the 7 d back trajectory:

$$\Delta\text{CO}_{2,\text{mod}} = \sum_{0\text{h}}^{-168\text{h}} \sum_{ij} \text{foot}_{ij} \times (\text{ANTH}_{ij} + \text{VPRM}_{ij}). \quad (2)$$

Note that for the modeled enhancement or depletion, only the VPRM fluxes change hourly; as stated previously, the annual anthropogenic fluxes are atemporal.

Without a sufficiently dense network of high-temporal-resolution observations, a full-scale inverse modeling approach to inventory scaling is inappropriate. At annual timescales, where anthropogenic sources dominate the CO₂ signal, we compare annual observed and modeled ΔCO₂ to define a mean bias and derive a scale factor to quantify the model–observation mismatch based on the slope of the comparison. Isotopic analysis of atmospheric CO₂ from a site in Beijing in 2014 suggests that annually the fossil fuel burning does dominate the region, contributing 75 % ± 15 % to the annual signal (Niu et al., 2016). Annually, the biospheric impact in the region is not zero; rather, the anthropogenic signal dominates. The biospheric quantity of relevance annually is the net carbon flux as a balance of GPP and respiration and is highly uncertain in both sign and magnitude in this region (Piao et al., 2009). In the Piao et al. (2009) study, regional inversions are based on the very limited dataset of nine sites across all of Asia. Our assumption of dominant anthropogenic influence in northern China is in keeping with the priors and process-based models from the relevant regions in Piao et al. (2009) that assume zero and are not significantly corrected by relatively poorly constrained inversions. At seasonal timescales, we use the difference between observed and modeled ΔCO₂ normalized by L_{0.90} area to obtain a mass flux offset that combines vegetation and anthropogenic inventories. With the available data it is not possible to independently evaluate both the anthropogenic and biogenic CO₂ fluxes. For further details of the scaling technique, please refer to Sect. S5.

Uncertainty analysis

The sources of uncertainty in calculations of ΔCO₂ include uncertainty in CT2015 background concentrations, CO₂ observations, STILT footprints, anthropogenic inventories, and the biogenic CO₂ fluxes from the VPRM. We obtain 95 % confidence bounds for ΔCO₂ by following a procedure similar to McKain et al. (2015) and Sargent et al. (2018) that involves bootstrapping daily averages of hourly afternoon values. For monthly and seasonal timescales, we obtain 95 % confidence intervals for ΔCO_{2,obs} by performing a bootstrap on probability distributions of errors in both the CT2015 and observations 1000 times. (See Sect. S4 and Fig. S9 for details on parameterizing CT2015 uncertainty.) The relevant quantiles are obtained from the resulting distribution, and are reported relative to the mean ΔCO_{2,obs} of the original data subset. We follow a slightly modified approach for ΔCO_{2,mod} in that we construct monthly and seasonal residual pools from daily averages of hourly afternoon CO_{2,mod} – CO_{2,obs}. The residuals – the deviation of the model from the true observed values – represent the total uncertainty in the model and therefore aggregate the effects of uncertainty in the footprints, background, and inventories. Monthly and seasonal 95 % confidence intervals of CO_{2,mod} – CO_{2,obs} are then obtained from the distribution of bootstrapping the residual pools 1000 times. We then obtain the mean and 95 % confidence interval of ΔCO_{2,mod} by applying the relevant quantiles of the residuals to the mean ΔCO_{2,obs} of the original data subset. Similar to Sargent et al. (2018) and McKain et al. (2015), distributions of seasonal averages obtained from the above method are used to estimate annual averages and 95 % confidence intervals.

Sargent et al. (2018) note that applying the same meteorological model over a long time period (15 months) allows for detection of trends in transport uncertainty. In this study, the drawback of a single location is offset somewhat by a much longer time series (60 months). Absent a dense network of observations, a more sophisticated and extensive error analysis cannot be conducted with meaningful results. Turnbull et al. (2011) faced a similar issue, where weekly flask data collected between 2004 and 2010 from two sites in the NOAA ESRL/WMO sampling network were used to evaluate a bottom-up fossil inventory based on CDIAC and EDGAR estimates. Turnbull et al. (2011) noted the difficulty in assessing the transport error given the paucity of regional observations but also demonstrate the power of top-down assessments given improvements in regional transport modeling and density of observations.

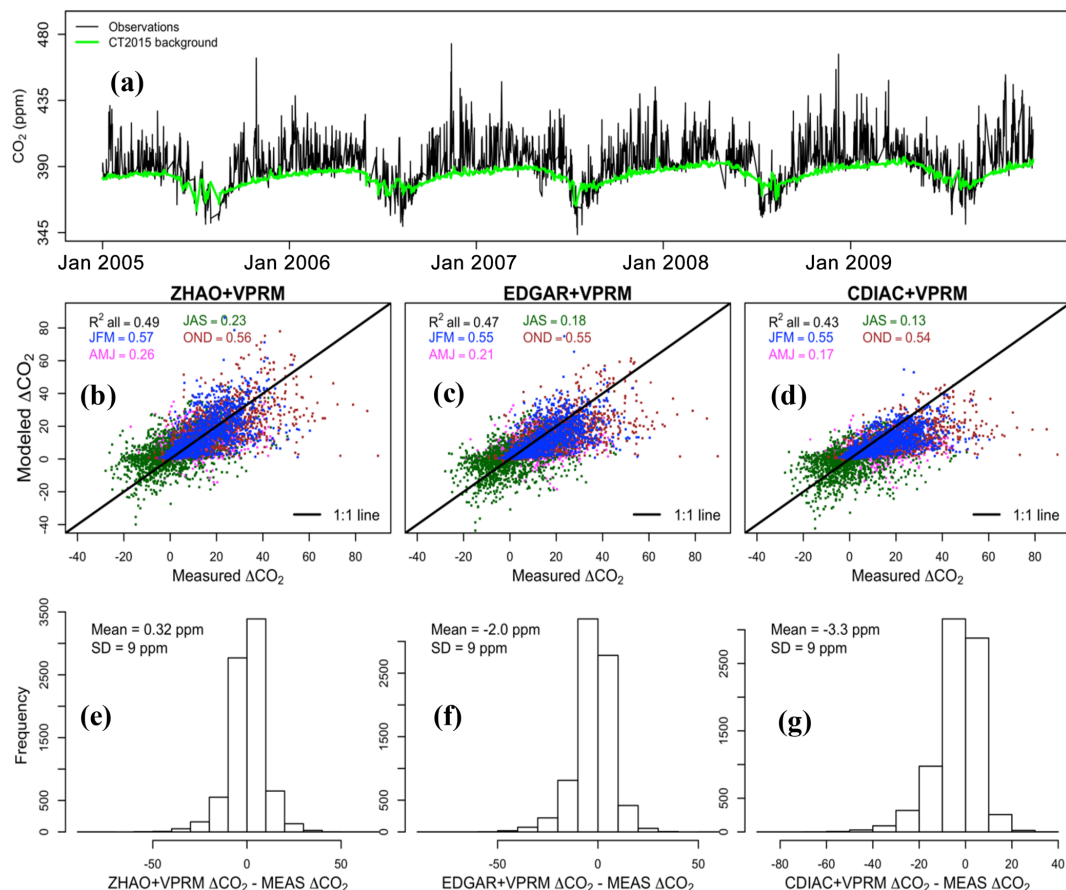


Figure 3. Hourly (11:00 to 16:00 LT) modeled and measured CO₂ and ΔCO₂. Measured CO₂ and modeled CT2015 background concentrations are displayed in (a). Modeled versus measured ΔCO₂ for each anthropogenic inventory is shown in (b)–(d), colored by season. Histograms of modeled and measured residuals are shown in (e)–(g). The VPRM vegetation component is included in all modeled ΔCO₂ values.

4 Results and discussion

4.1 Impact of seasonality on evaluation region

As shown in Fig. 2, we find strong seasonality in the footprint percentile contours, in agreement with previous analysis of Miyun observations by Wang et al. (2010). At annual timescales, the L_{0.90} region is comparable to the WRF d02 extent. Northern China, including Inner Mongolia, dominates the L_{0.90} region both seasonally and annually. Due to the heavy biosphere influence in the regional growing season, previous work by Wang et al. (2010) used Miyun non-growing-season measurements of CO₂ and carbon monoxide (CO) as an anthropogenic tracer to estimate combustion efficiency for China. When compared to bottom-up estimates of national combustion efficiency, observations suggested 25 % higher combustion efficiency than bottom-up estimates of national combustion efficiency; however, Wang et al. (2010) note that the regional (northern China) and seasonal (winter) subsets could contribute to such a discrepancy. The seasonality exhibited in Fig. 2 indeed suggests that combustion

efficiency estimates derived from non-growing-season measurements alone do not represent anthropogenic processes in provinces south of Miyun that are visible in the observations primarily during the growing season. Low-emitting regions northwest of Miyun such as Inner Mongolia influence the site more in the fall and winter relative to other seasons. In the spring and summer, higher-emitting regions in provinces south of Miyun are more influential. However, non-growing-season CO₂ is influenced by often inefficient district heating in the northwest. And, while growing-season CO₂ is influenced by intense urban activities from Beijing and other cities to the south, vegetation draws down both background and locally observed CO₂ significantly (Fig. 3a).

4.2 Unscaled models: performance at multiple timescales

We evaluate unscaled model performance relative to observations at hourly, seasonal, and annual timescales. While inventory scaling is performed at the policy-relevant scales of seasons and years, examination of the models at shorter

Table 1. Quantification of model–observation mismatch at hourly timescales averaged over 2005–2009 and pooled by season (W = winter; Sp = spring; Su = summer; F = fall). We provide standard major axis (SMA) slopes and 95 % confidence intervals, R^2 quantities (those > 0.2 are in bold), and mean bias and root mean square error (RMSE) in ppm.

SMA slope (95 % CI)					
	All	W (JFM)	Sp (AMJ)	Su (JAS)	F (OND)
$\Delta\text{CO}_2_{\text{ZHAO+VPRM}}$	0.89 (0.88,0.91)	1.0 (1.0,1.1)	0.74 (0.72,0.77)	0.88 (0.84,0.92)	0.92 (0.90,0.95)
$\Delta\text{CO}_2_{\text{EDGAR+VPRM}}$	0.77 (0.76, 0.78)	0.83 (0.81, 0.86)	0.62 (0.60, 0.65)	0.83 (0.80, 0.87)	0.77 (0.74, 0.79)
$\Delta\text{CO}_2_{\text{CDIAC+VPRM}}$	0.63 (0.62, 0.64)	0.63 (0.62, 0.65)	0.48 (0.46, 0.50)	0.79 (0.75, 0.82)	0.56 (0.54, 0.58)
R^2					
	All	W (JFM)	Sp (AMJ)	Su (JAS)	F (OND)
$\Delta\text{CO}_2_{\text{ZHAO+VPRM}}$	0.49	0.56	0.26	0.22	0.56
$\Delta\text{CO}_2_{\text{EDGAR+VPRM}}$	0.47	0.55	0.21	0.18	0.55
$\Delta\text{CO}_2_{\text{CDIAC+VPRM}}$	0.43	0.55	0.17	0.13	0.54
Mean bias (RMSE), ppm					
	All	W (JFM)	Sp (AMJ)	Su (JAS)	F (OND)
$\Delta\text{CO}_2_{\text{ZHAO+VPRM}}$	0.32 (9.2)	0.014 (7.9)	−0.033 (8.3)	3.1 (11)	−1.1 (9.7)
$\Delta\text{CO}_2_{\text{EDGAR+VPRM}}$	−2.0 (9.3)	−2.2 (7.7)	−1.9 (8.7)	0.25 (10.8)	−3.4 (10.1)
$\Delta\text{CO}_2_{\text{CDIAC+VPRM}}$	−3.3 (9.9)	−3.1 (8.1)	−3.3 (9.2)	−1.1 (11.3)	−5.0 (11.1)

timescales provides insight into model bias and error aggregation at longer timescales. Table 1 summarizes hourly model bias across all years and pooled by season.

All modeled hourly quantities include the same biological component from VPRM, background concentrations, and transport models such that the only source of variation among models is the anthropogenic inventory. With a few exceptions that are discussed in the following sections, $\text{CO}_2_{\text{EDGAR+VPRM}}$, $\text{CO}_2_{\text{CDIAC+VPRM}}$, $\Delta\text{CO}_2_{\text{EDGAR+VPRM}}$, and $\Delta\text{CO}_2_{\text{CDIAC+VPRM}}$ systematically underestimate observations, as indicated by larger deviation below the 1 : 1 line in the comparison of modeled to measured ΔCO_2 (Table 1, Fig. 3b–d.)

4.2.1 Hourly

We examine the distribution of modeled-measured residuals at hourly timescales for each anthropogenic inventory. While standard deviations are consistent across all models of CO₂ flux ($1\sigma = 9$ ppm; Fig. 3e–g) $\Delta\text{CO}_2_{\text{ZHAO+VPRM}}$ exhibits the least bias relative to observations with a mean residual of 0.32(0.12, 0.53) ppm. In contrast, $\Delta\text{CO}_2_{\text{EDGAR+VPRM}}$ and $\Delta\text{CO}_2_{\text{CDIAC+VPRM}}$ display significantly greater bias by typically underestimating observations by large amounts: −2.0(−1.8, −2.2) ppm and −3.3(−3.1, −3.5) ppm, respectively. Here, the 95 % confidence intervals are derived from a two-sample t test. The EDGAR and CDIAC underestimation of ΔCO_2 at the hourly scale is consistent across longer timescales of seasons and years, as discussed in the following sections, but we note where there are likely aliased effects of the uncertainty in the VPRM biogenic component.

4.2.2 Seasonal

The seasonally averaged modeled and measured ΔCO_2 values shown in Fig. 4 illustrate the overall biases for the four inventories. Outside of June, July, August, and September, the anthropogenic signal dominates in northern China (Wang et al., 2010). We see from Table 1 that during seasons where biological activity is lower or significantly lower than anthropogenic activity, there is a consistent discrepancy among the CO₂ modeled by the three different anthropogenic inventories suggesting systematic differences largely attributable to the anthropogenic component (as we do not vary any other component). In the fall, where respiration is the dominant biological process, all three modeled quantities are consistently lower than observations – a likely a consequence of the known underestimate of ecosystem respiration by the VPRM (Dayalu et al., 2018a). Even so, China's significant anthropogenic component still dominates during these months. During the winter season, where all biospheric activity is at a minimum, the model–observation mismatch is most reflective of biases among anthropogenic inventories rather than aliased impacts from the VPRM. As shown in the winter data in Table 1, ZHAO displays the least bias relative to observations (0.01 ppm), followed by EDGAR (−2.2 ppm) and CDIAC (−3.1 ppm).

With the exception of the peak JAS growing season, $\Delta\text{CO}_2_{\text{EDGAR+VPRM}}$ and $\Delta\text{CO}_2_{\text{CDIAC+VPRM}}$ typically underestimate $\Delta\text{CO}_2_{\text{OBS}}$, even within the 95 % uncertainty bounds. The VPRM has a limited calibration network that contributes to an underestimate of regional CO₂ drawdown during the growing season (Dayalu et al., 2018a). Therefore,

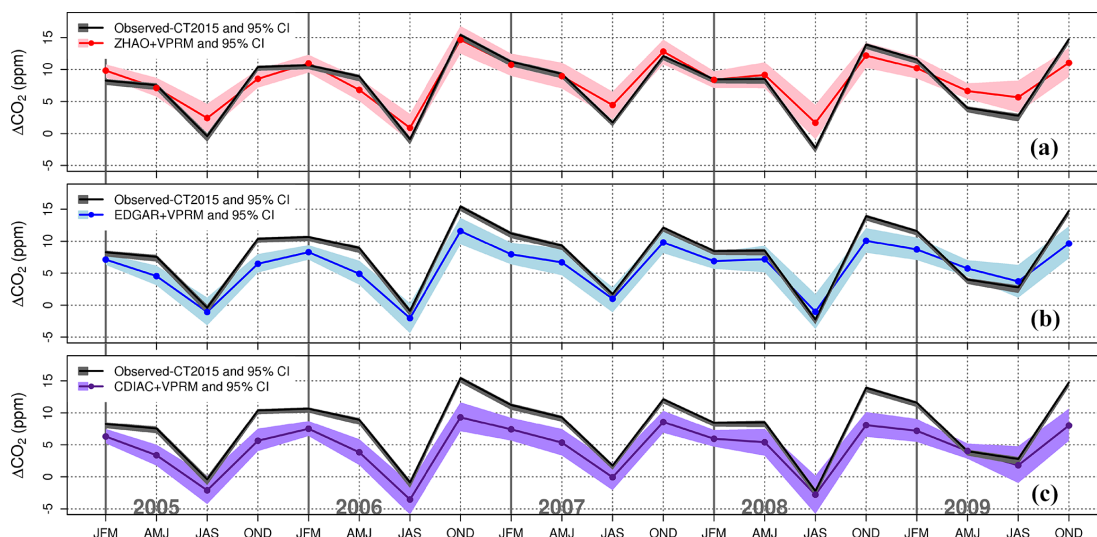


Figure 4. Modeled and measured seasonal ΔCO_2 . CT2015 background is subtracted from observations to provide observed ΔCO_2 (black line), and 95 % confidence bounds are derived from bootstrapping hourly afternoon concentrations for each season.

while $\Delta\text{CO}_{2,\text{ZHAO}+\text{VPRM}}$ agrees within 95 % confidence bounds with $\Delta\text{CO}_{2,\text{OBS}}$ during the non-growing seasons, $\Delta\text{CO}_{2,\text{ZHAO}+\text{VPRM}}$ generally overestimates CO₂ concentrations in the growing season (Fig. 4a). $\Delta\text{CO}_{2,\text{EDGAR}+\text{VPRM}}$ (Fig. 4b) and $\Delta\text{CO}_{2,\text{CDIAC}+\text{VPRM}}$ (Fig. 4c) display lower CO₂ concentrations and generally result in better agreement with observations during the peak growing season than at other times of the year; however, our wintertime and overall analysis at hourly timescales (Fig. 4, Table 1) suggests this is an artifact of lower anthropogenic emissions estimates relative to ZHAO that counteracts the VPRM underestimating drawdown. Even during the growing season, $\Delta\text{CO}_{2,\text{CDIAC}+\text{VPRM}}$ agrees with observations typically at its upper confidence limits. However, during times of the year where the impacts of underestimated respiration become more significant (e.g., Fall) it is possible that the seemingly better agreement of ZHAO + VPRM is linked to a counteracting effect of overestimated anthropogenic emissions.

As ZHAO + VPRM demonstrates the least bias relative to observations at hourly and seasonal scales, we model the relative contributions to the monthly signal during the May through September peak regional growing season as defined by Wang et al. (2010). Figure 5 displays the results from partitioning the mean monthly $\Delta\text{CO}_{2,\text{ZHAO}+\text{VPRM}}$ signal as a multi-year average into anthropogenic and vegetation contributions. While the WRF-STILT-VPRM framework has been successfully adapted for similar CO₂ inventory evaluation studies in North American regions where biogenic fluxes dominate surface processes (Karion et al., 2016; Matross et al., 2006), Fig. 5 shows the relative magnitude of biogenic fluxes and anthropogenic emissions in the northern China region is comparable during peak summer, making it difficult to independently constrain them with observational data. As

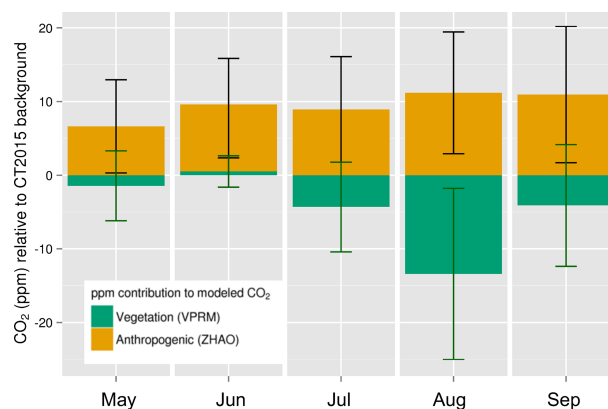


Figure 5. Modeled mean monthly contribution (ppm) to Miyun CO₂ concentrations from vegetation (VPRM) and anthropogenic (ZHAO) sources. Enhancement and depletion are relative to advected CT2015 background concentrations during the regional growing season (MJJAS), averaged over 2005 to 2009. Vertical lines represent 1 σ of monthly averages (green: vegetation; black: anthropogenic). Negative values represent depletion from CT2015 background; positive values represent enhancement of CT2015 background.

noted in Sect. 3, the regional peak uptake during the growing season occurs with the onset of the corn growing season around July and August. The atypical lower uptake during June represents the winter wheat to corn transition period. These results are consistent with the biological component estimated by Turnbull et al. (2011). Furthermore, knowledge of the relative contribution of vegetation and anthropogenic processes to the CO₂ signal during the peak growing season is necessary to interpret satellite retrievals of CO₂ over the region (Dayalu et al., 2018a).

4.2.3 Annual

Aggregation of uncertainty and anthropogenic inventory biases at shorter timescales becomes most apparent at the annual timescales. For annual budgeting we follow the assumptions of Piao et al. (2009) and Jiang et al. (2016) that agricultural systems are in annual carbon balance because crop biomass has a short residence time. In the absence of data on regional transfer of agricultural products and proportion of grains used in situ for livestock vs. human consumption in China this is the most conservative assumption to make. Given the dense population in most of Beijing province we expect there may be net import of agricultural products from outside the L_{0.90} region, which would show up as additional respiration not captured by VPRM, but that term will be small relative to the anthropogenic CO₂ (Fig. 5) (Dayalu et al., 2018a). Therefore, while the VPRM is implicitly included in the modeled annual CO₂ and ΔCO₂, vegetation carbon stocks (including harvested products and crop residues) from the portions of the L_{0.90} region with widespread agriculture largely turn over such that only the anthropogenic inventories dominate the modeled CO₂ signal. We evaluate annual CO₂ including CT2015 background (Fig. 6a–c) and as regional enhancement relative to background (Fig. 6d–f). We show that for all years, CO_{2,ZHAO+VPRM} and ΔCO_{2,ZHAO+VPRM} agree tightly within 95 % uncertainty to observations (Fig. 6a and d). EDGAR + VPRM and CDIAC + VPRM are consistently biased significantly lower than observations.

4.3 Evaluation of inventories at seasonal and annual timescales

We quantify model–observation mismatch by estimating the additive flux corrections at seasonal timescales and multiplicative corrections at annual timescales. We emphasize that these “corrections”, or scalings, are not optimizations; rather, they simply reflect the extent to which the individual anthropogenic + VPRM flux models deviate from the observations. Complete seasonal and annual scaling results are provided in Sect. S5 and Tables S2–S3.

The observational record informing the scaling integrates the biological and anthropogenic signals. At the seasonal scale, where biological processes are significant contributors to the signal, we scale the sum of the anthropogenic and biological fluxes (Fig. 7). Scaled non-growing-season flux estimates are higher than unscaled values, partially accounting for the VPRM generally underestimating ecosystem respiration by an additive offset throughout the year (Dayalu et al., 2018a). The multi-year seasonal results in Table 1 suggest that this offset can aggregate to a 1–2 ppm difference; the result would be a shift in baseline rather than overall pattern for each of the three simulations. As the vegetation and all other components are controlled across models, the inter-model variance reflects the relative per-

Table 2. Annual scaling factors (95 % CI) and corresponding corrected emissions for the L_{0.90} inventory evaluation region.

		Scaling factor (95 % CI)	Corrected emissions, MtCO ₂ (95 % CI)	Original emissions, MtCO ₂
2005	ZHAO	0.95 (0.84, 1.0)	2800 (2476, 3105)	3015
	EDGAR	1.4 (1.3, 1.6)	3306 (2886, 3683)	2322
	CDIAC	1.7 (1.5, 1.9)	3489 (3017, 3871)	1930
2006	ZHAO	1.0 (0.91, 1.1)	3326 (2972, 3631)	3273
	EDGAR	1.5 (1.3, 1.6)	3751 (3325, 4150)	2586
	CDIAC	1.9 (1.6, 2.0)	3930 (3438, 4338)	2160
2007	ZHAO	0.94 (0.85, 1.0)	3080 (2789, 3324)	3588
	EDGAR	1.4 (1.2, 1.5)	3454 (3096, 3785)	2799
	CDIAC	1.6 (1.5, 1.8)	3180 (2842, 3493)	2260
2008	ZHAO	0.94 (0.82, 1.0)	3422 (3008, 3768)	3685
	EDGAR	1.2 (1.1, 1.4)	3790 (3332, 4207)	3095
	CDIAC	1.7 (1.5, 1.9)	3941 (3461, 4374)	2395
2009	ZHAO	0.96 (0.86, 1.1)	3860 (3474, 4251)	3974
	EDGAR	1.1 (1.0, 1.3)	3518 (3133, 3874)	3298
	CDIAC	1.5 (1.3, 1.7)	3921 (3454, 4330)	2543

formance of the anthropogenic estimates. We find that in the non-growing months the original ZHAO + VPRM inventory typically remains within the 95 % confidence bounds of the scaled inventory. However, both EDGAR + VPRM and CDIAC + VPRM are consistently significantly lower than their scaled counterparts. At least in the winter, where biogenic processes are at a minimum, this suggests that both EDGAR and CDIAC underestimate anthropogenic emissions, and that ZHAO estimates are closer to actual emissions. Improved representation of temporal anthropogenic activity factors and biosphere processes are needed to extend the conclusions of anthropogenic inventory performance to all seasons. In the absence of such data, it is not possible to conclusively state whether model–data mismatch is rooted in anthropogenic emissions biases or biogenic biases. During the growing seasons, however, the afternoon vegetation signal is significant, and the picture is more complex. In the spring, the CO₂ signal at Miyun is significantly affected by the North China Plain winter wheat growing season. The effect of scaling in the spring from 2005 to 2007 is to increase CO₂ emissions with a net positive seasonal flux; however, in 2008 and 2009 we find the net seasonal flux becomes negative such that uptake dominates emissions. The prior models in all cases predict positive flux. During the summer months, ZHAO + VPRM predicts more emissions and/or less uptake relative to EDGAR + VPRM and CDIAC + VPRM. Scaling of summertime fluxes serves to significantly increase ZHAO + VPRM uptake estimates; the EDGAR + VPRM and CDIAC + VPRM prior estimates are within the 95 % confidence bounds of the scaling for reasons discussed previously.

We report annual scaled anthropogenic inventories in the L_{0.90} region in Fig. 8 and Table 2 as MtCO₂ yr⁻¹. As dis-

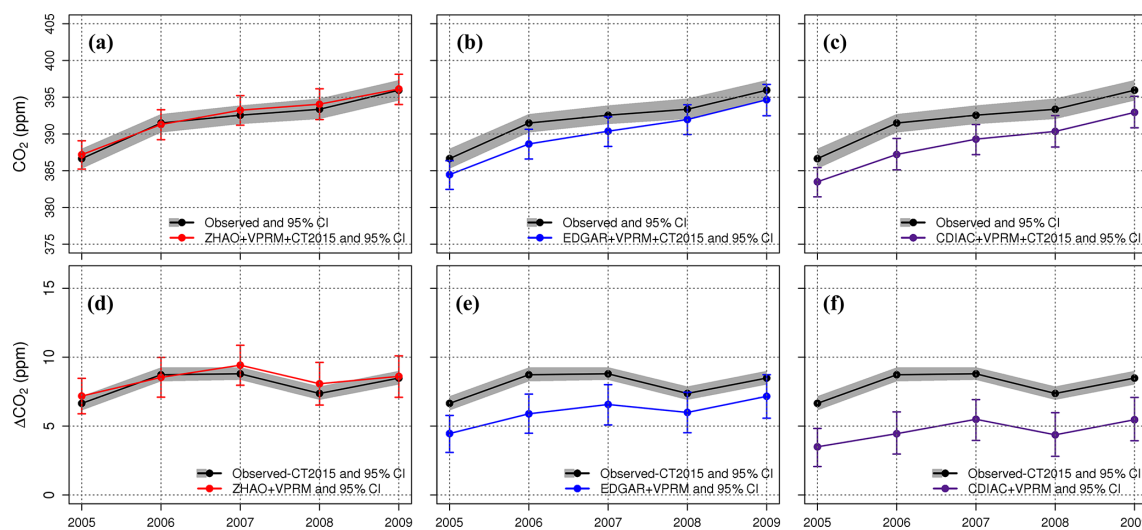


Figure 6. Mean annual CO₂ and ΔCO₂ over the entire study time period. (a–c) CO₂ annual concentration; (d–f) ΔCO₂ (regional enhancement, after removal of advected CT2015 background) with bootstrapped 95 % confidence intervals.

cussed previously, the annual scalings are applied only to the anthropogenic inventory, as the signal at the annual timescale is effectively dominated by anthropogenic emissions; net ecosystem fluxes are expected to be relatively minor in the L_{0.90} region in comparison. For all years, the emissions estimated by the original ZHAO inventory lie within the 95 % confidence bounds of the scaled ZHAO inventory. However, for EDGAR and CDIAC, the original inventories consistently underestimate observations. Averaged over the 5-year study period, EDGAR and CDIAC lead to modeled estimates of CO₂ mixing ratios that are typically lower than observations by 30 % and 70 % respectively (Fig. 6). Averaged across the 5 years, this translates to EDGAR and CDIAC being scaled relative to their unscaled values in the L_{0.90} region by 1.3 and 1.7, respectively (Fig. 8; Table 2). In the case of EDGAR, we note a general increase in observational agreement from 2005 to 2009.

4.4 Potential contributions to regional carbon emissions patterns from 2005 to 2009

We examine the statistical significance of the inter-annual observed concentration and enhancement differences using a two-sample *t* test (Table 3). The observed concentrations including advected global background (Fig. 6a–c) display an overall increasing trend of 1.87 (1.8, 1.9) ppm CO₂ yr⁻¹ between 2005 and 2009, in agreement with flask samples obtained from nearby WMO sites between 2007 and 2010 (Liu et al., 2015). The inter-annual increases are statistically significant (Table 3). However, when we remove the modeled background to more closely examine regional patterns that would otherwise be drowned out by the global signal, we find that the regional ΔCO₂ trend (Fig. 6d–f; Table 3) does not parallel the increasing global CO₂ trend (Fig. 6a–c; Table 3).

Regionally, the observed enhancements increase from 2005 to 2006 and plateau in 2007 before decreasing in 2008. Regional ΔCO₂ increases again in 2009. Earlier work by Wang et al. (2010) extended the Miyun observations of CO₂ growth rate to all of China and estimates a lower CO₂ growth rate than previously suggested. However, Fig. S6 suggests local reductions in regions influencing Miyun, possibly in preparation for the Beijing Olympics, are partially offset by increases elsewhere. A larger network of sites would be needed to quantify this further in order to evaluate the CO₂ growth rate for other regions in China and for China as a whole.

In Fig. 9a we estimate gross regional product (GRP) for 8 of China's 34 provincial-level administrative units, specifically those encompassed significantly by the L_{0.90} region: Beijing, Tianjin, Henan, Shanxi, Shandong, Hebei, Inner Mongolia, and Liaoning. Using data from the International Monetary Fund (IMF; <https://www.imf.org/en/Data>, last access: 9 February 2020) and World Bank (World Bank, 2017) we retrieved the GDP for each of the above provinces and summed them to estimate the GRP. GDP calculations are inherently uncertain and were available as single values for each province per year. A more extensive economic analysis to estimate the uncertainty of these values is beyond the scope of this study. Key economic events occurred during the study time period and are likely contributors to the observed interannual variation in regional CO₂ emissions (Fig. 6d–e) and a doubling of GRP from 2005 to 2009 (Fig. 9a). In particular, the time period from 2005 to 2009 saw industrial energy efficiency improvements which began in 2007 under the 11th FYP, preparations for and staging of the 2008 Beijing Summer Olympics, the global financial crisis in late 2008, and a large Chinese fiscal stimulus in 2009. We further note that the global financial crisis of 2008 correlates with a plateau-

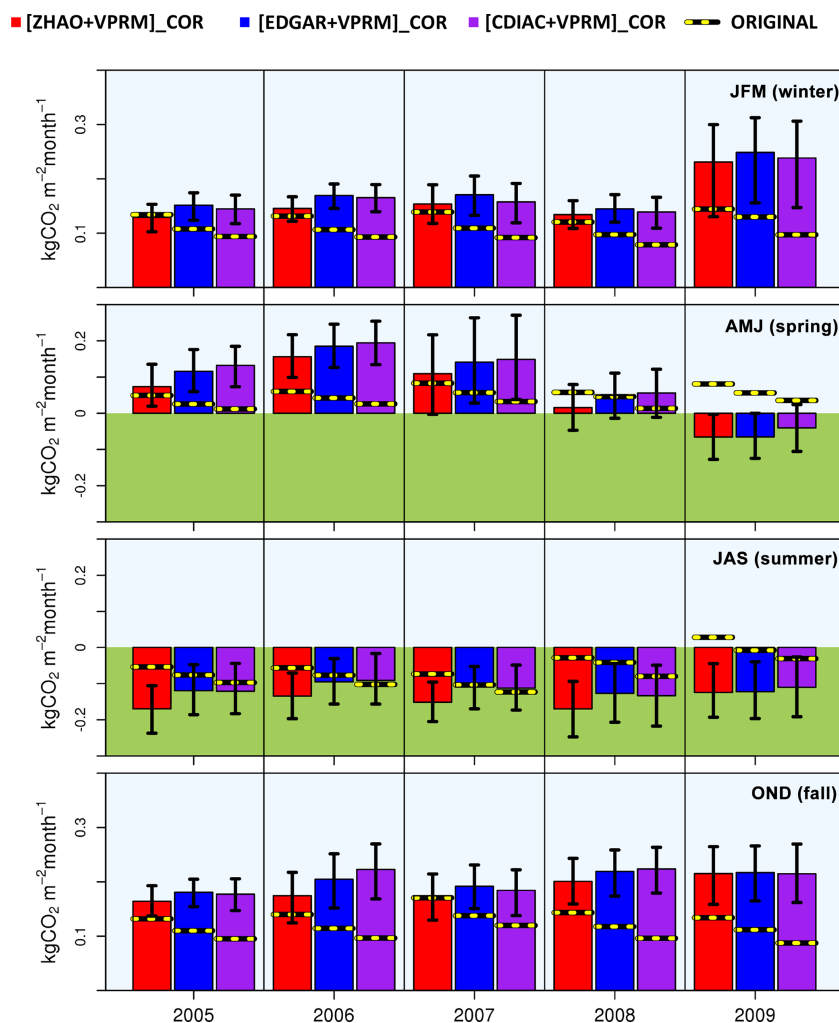


Figure 7. Scaled seasonal fluxes in the L_{0.90} region ($\text{kg CO}_2 \text{ m}^{-2}$ per month). Anthropogenic and vegetation inventories are scaled together ([ANTH+VPRM]_{COR}). The black and yellow dashed line is the seasonal flux estimated by the original ANTH+VPRM model. All models have the same vegetation component (VPRM) and differ only in the anthropogenic inventory source. Shaded green represents negative flux (uptake by biosphere). The scaling based on additive corrections; the difference among scaled inventories is due to differing spatial allocations by anthropogenic inventories. Bootstrapped 95 % confidence intervals are represented by the black vertical lines.

ing of the percentage contribution of northern China GRP to national GDP (Fig. 9a).

As policy targets are often measured as relative changes over multiple years, an important component of emissions inventories is their ability to accurately capture multi-year changes. Observations indicate enhancements above background CO₂ increased by 28 % (22 %, 34 %) between 2005 and 2009. ZHAO + VPRM estimates a 20 % increase over the same time period while EDGAR + VPRM and CDIAC + VPRM estimate 61 % and 56 % increases respectively.

Table 3. Inter-annual observed CO₂ and ΔCO_2 differences. Differences are of observations between consecutive years. The 95 % confidence intervals are derived from a two-sample *t* test. Italicized entries denote instances where the inter-annual difference is not statistically significant (confidence interval includes zero).

Time interval ($y_2 - y_1$)	CO ₂ ,OBS (ppm) mean difference (95 % CI)	ΔCO_2 ,OBS (ppm) mean difference (95 % CI)
2006–2005	4.86 (4.5, 5.2)	2.08 (1.9, 2.3)
2007–2006	1.08 (0.69, 1.5)	<i>0.0693 (−0.15, 0.29)</i>
2008–2007	0.772 (0.37, 1.2)	−1.43 (−1.6, −1.2)
2009–2008	2.60 (2.2, 3.0)	1.12 (0.88, 1.4)
2009–2005	9.31 (8.9, 9.7)	1.84 (1.6, 2.0)

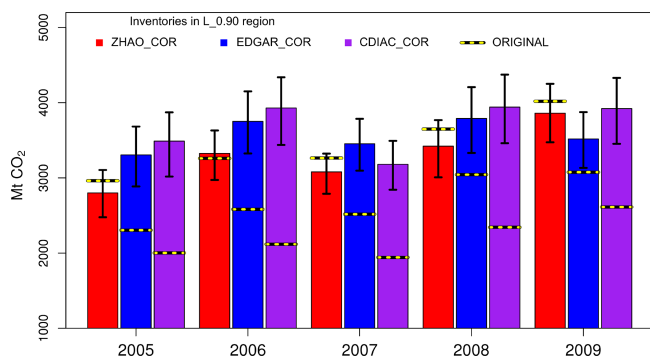


Figure 8. Annually scaled emissions in the L_{0.90} region. Scaling is based on multiplicative scaling factors. Difference among scaled inventory means is due to differing spatial allocations in original anthropogenic inventories. Bootstrapped 95 % confidence intervals are represented by the black vertical lines. * Note the y axis origin begins at 1000 Mt CO₂ for visual clarity.

4.5 Implications for assessing national carbon emission targets

China has pledged a 60 %–65 % reduction in carbon intensity by 2030 and has additionally set a benchmark of 40 %–45 % reduction in carbon intensity by 2020, where both targets are relative to the baseline year 2005 (NDRC, 2015; Guan et al., 2014). However, Guan et al. (2014) found that provincial trends in carbon intensity can vary significantly from national trends. Using the GRP values shown in Fig. 9a, we calculate a northern China regional carbon intensity incorporating the eight provinces encompassed significantly by the L_{0.90} region (Fig. 9c). We also estimate an L_{0.90} regional carbon intensity based on the official national energy-related CO₂ emissions in NDRC (2015); we scale the national total by 39 % (35 %, 42 %), which is the mean (range) contribution of the L_{0.90} region to the national emissions in 2005, averaged across the three unscaled gridded emissions inventories. We emphasize that carbon intensity values are inherently uncertain due to complexities in GRP and GDP calculations such as double-counting due to inter-provincial trade or spatial mismatch between emissions and economic data. Nevertheless, the analysis provides valuable insight into trends rather than precise values.

Over the study time period, the GRP of the L_{0.90} region more than doubled (Fig. 9a), exhibiting a moderate, positive correlation with the increasing trend in emissions (Fig. 9b). Coinciding with the 2008 Beijing Summer Olympics, the region's contribution to China's GDP grew from approximately 13.5 % in 2007 to nearly 16 % in 2008, representing a 20 % increase, before plateauing into 2009 (Fig. 9a). As noted in Guan et al. (2014), reductions in carbon emissions intensity can come about via two main pathways: the first, within industries, through increased energy efficiency combined with expanded production capacity; the second, across the economy, through structural shifts from energy-intensive

industrial sectors to service sectors. The doubling of GRP with the apparent reduction in regional carbon intensity suggests a combination of enlarged production capacity (including production of higher valued goods) and a shift toward a service-oriented economy. In the former instance, a larger production capacity tends to reduce the overall energy (and, therefore, carbon) consumption of a single production unit. In the latter instance, the energy consumption by the service sector is considerably lower than that required by industrial and manufacturing processes. In the northern China region, however, industry continues to dominate the economy, suggesting that carbon intensity reductions are more due to enlarged production capacity. From 2005 to 2009, carbon intensity for the L_{0.90} region decreased by 47 % (28 %, 65 %), based on a one-sample *t* test of pooled emissions intensity changes across scaled inventories. Analysis presented by organizations such as the World Bank (World Bank, 2017) suggests China's carbon intensity at the national level decreased by 20 % in 2009 relative to 2005. However, we note that the carbon emissions data source for the World Bank carbon intensity calculations is CDIAC. We have shown that at least for the L_{0.90} region, CDIAC emissions lead to significant underestimates of observations. Our work here suggests that carbon accounting organizations such as the World Bank would benefit from basing their national estimates for China on a variety of inventories, incorporating increasingly available China-specific approaches (including but not limited to MEIC and PKU), EDGAR, and newer global inventories such as ODIAC. However, we emphasize a crucial point with respect to the value of carbon intensity targets, in agreement with Guan et al. (2014): carbon intensity targets are especially misleading in developing countries where absolute emissions continue to significantly grow in concert with economic development goals. We see that despite the decreasing carbon intensity of the region, pooled emissions estimates from the three scaled inventories suggest an 18 % increase in absolute emissions from 2005 to 2009 (Table 2, Fig. 9b). In terms of the climate impact, it is the absolute carbon emissions rather than the carbon intensity that ultimately matters.

5 Conclusions

Continuous hourly CO₂ observations, significantly influenced by the heavily CO₂-emitting northern China region, are used in a top-down evaluation and scaling of three bottom-up CO₂ flux inventories. We focus on the policy-relevant time interval from 2005 to 2009, noting that 2005 is China's baseline year for carbon commitments. The three inventories are distinct in their anthropogenic component, with a common biogenic flux component provided by the VPRM, a simple satellite data-driven biosphere model calibrated with ground-level ecosystem observations. The ZHAO anthropogenic emissions inventory incorporates a regional approach to China's CO₂ emissions estimation, using activity

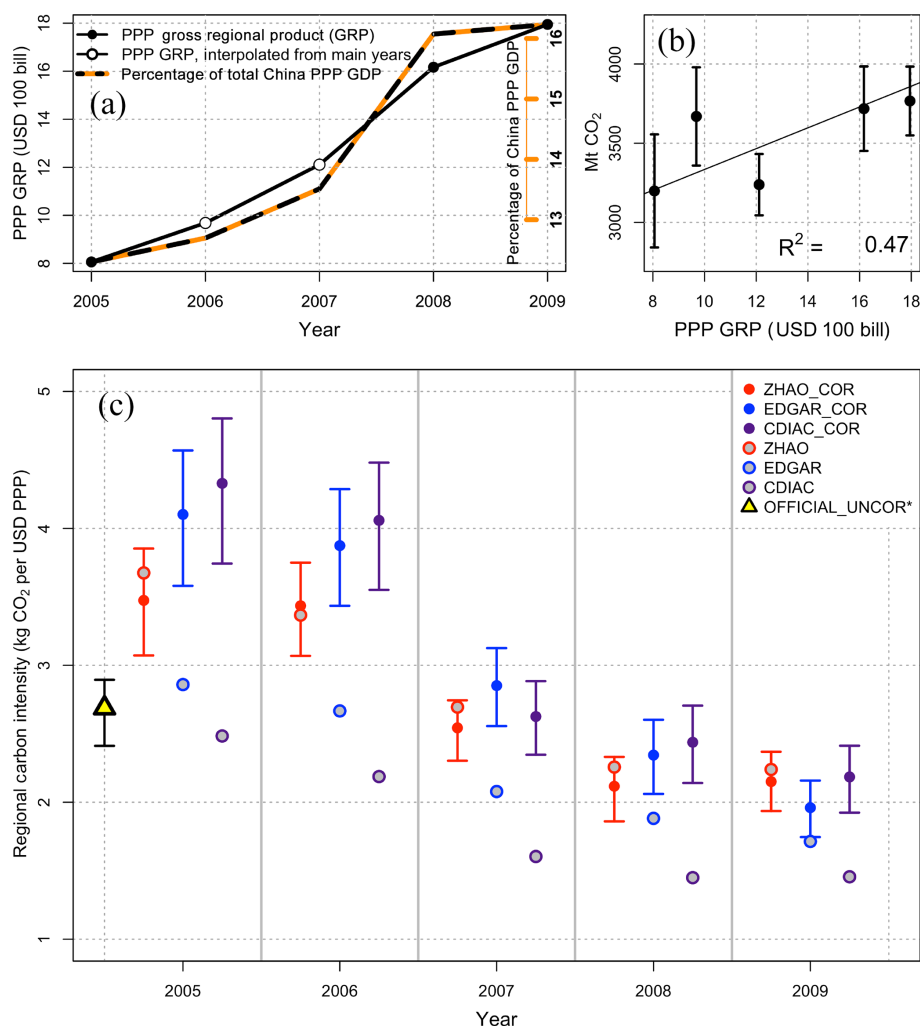


Figure 9. Estimates of regional carbon intensity (kg of CO₂ per USD). (a) PPP GRP by year and as a percentage of China's national GDP. No PPP GRP values were available for 2006 and 2007; PPP GRP for these years was derived from a linearly interpolated ratio of nominal GRP/PPP GRP for 2005, 2008, and 2009. (b) Correlating corrected regional emissions from Table 2 with PPP GRP; values are pooled annual means among ZHAO, EDGAR, and CDIAC with 1σ error bars. (c) Regional carbon intensity using scaled (solid) and unscaled (grey) CO₂ estimates. Error bars are bootstrapped 95 % confidence intervals. GRP and GDP data are from the IMF and World Bank. Provinces used in GRP calculation are those significantly encompassed by the L_{0.90} region: Beijing, Henan, Shanxi, Tianjin, Shandong, Hebei, Inner Mongolia, and Liaoning. * Estimated by scaling the official national emissions total by the average contribution (39 %) of the L_{0.90} region to total emissions in 2005. Uncertainty bars represent the percentage contribution range estimated by ZHAO, EDGAR, and CDIAC in 2005 (35 %, 42 %).

data at the provincial and facility levels as well as domestic emission factors. The EDGAR and CDIAC emissions inventories incorporate a greater reliance on global averages and China's national statistics and international default emission factors and depend more heavily on proxies (e.g., population) to allocate the emissions geographically. The three anthropogenic inventories represent a range of methods used to estimate emissions for China.

The northern China administrative region, excluding Inner Mongolia, dominates the L_{0.90} region, which is the region over which we distribute the model–observation mismatch (Fig. 2). We find strong seasonality in the L_{0.90} region; the

northwest features more strongly in the non-growing season and there is a more symmetric influence in the growing season. Within the L_{0.90} region, EDGAR and CDIAC are – on average across the 5 study years – lower than ZHAO by 20 % and 36 %, respectively. Across administrative regions, the highest discrepancy between the global and regional inventories is in northern China, where the ZHAO inventory estimates emissions that are on average 30 % higher than both EDGAR and CDIAC (Table S1).

We find the ZHAO + VPRM inventory generally agrees very closely with observations, often significantly better than the nationally referenced inventories at all timescales (hourly

through annually), with the exception of the peak growing season. During the peak growing season, the regional enhancement to background CO₂ concentrations is modeled as approximately zero, due to an agriculturally dominated vegetation signal that is equal in magnitude and opposite in sign to the anthropogenic signal (Dayalu et al., 2018a). While this agrees with previous work by Turnbull et al. (2011), in both that study and the present study the sparse data prevent a more conclusive statement about anthropogenic inventory performance during the regional growing season. At annual timescales, the anthropogenic signal dominates, and we find that emission rates from EDGAR and CDIAC lead to underestimated emissions in the northern China region by an average of 30 % and 70 %, respectively, averaged across all study years. We note that the discrepancy between the EDGAR-based time series and the observations generally decreases over the 5-year study period. In contrast, emission rates from the ZHAO inventory gives a priori results very close to observations throughout and is not significantly affected by the scaling: the error bars for the scaled estimates consistently include the original estimate. Note that the EDGAR and CDIAC inventories can differ from -10 % to -20 % relative to ZHAO in their national emissions totals (Table S1). The inventories evaluated here exhibit distinct differences in their ability to match observations. However, observational data from a network of sites strategically located in and around the eastern half of China would be required to (1) examine whether differences in spatial allocation approaches contribute to differences among the inventories and (2) conduct actual optimizations of the inventories.

We find that carbon intensity in the region has decreased by 47 % (28 %, 65 %) from 2005 to 2009, from approximately 4 kg of CO₂ per USD in 2005 to about 2 kg of CO₂ per USD in 2009 (Fig. 9c). However, we see that despite the decreasing carbon intensity of the region, there is an 18 % increase in absolute emissions over time, affirming the point made by Guan et al. (2014) that meeting carbon intensity targets in emerging economies can be at odds with making real climate progress (Table 2, Fig. 9b).

Despite the limitations of having data from a single site, this analysis demonstrates how a long time series of continuous observations can identify apparent overall biases in some inventories. Our results, while specific to northern China regional emissions in particular, also provide some insight into current methods of carbon emissions accounting for China as a whole. We emphasize that this work is intended to be a comparison of emission rates from a subset of anthropogenic CO₂ inventories over northern China that were readily available at the time this research began and is not intended to be an advocate or criticism of any single published inventory. Rather, we use a long 60-month continuous observational record to examine model–data mismatch in an important carbon-emitting region where local data are difficult to access and global datasets are forced to rely on the best available public data, which are not necessarily accurate as-

sumptions of China-specific activity. Second, while we recognize the height limitations – and therefore the footprint – of the Miyun receptor, its topographic advantage along with the low-productivity vicinity makes it similar to other short-tower sites suitable for regional analysis. In addition, a detailed assessment of uncertainty stemming from errors in transport, biogenic inventories, and inventory spatial allocation remains a challenge. Independent verification from concurrent aircraft measurements (for example) or multi-level inlet locations were not available to quantify the impact of absolute and relative inlet location on transport uncertainty. Finally, we emphasize our implied seasonal and annual “corrections”, or scalings, of modeled CO₂ relative to observations are not optimizations; rather, they simply reflect the extent to which the individual anthropogenic + VPRM CO₂ flux models deviate from the observations. At least in the winter, where biogenic processes are at a minimum, the low bias of ZHAO-modeled CO₂ concentrations suggests the ZHAO inventory is closer to actual emissions. However, improved representation of temporal anthropogenic activity factors and biosphere processes are needed to extend the conclusions of anthropogenic inventory performance to all seasons. Effectively evaluating and constraining inventory emissions rates at relevant spatial scales requires multiple stations of high-temporal-resolution observations, as well as improvements and greater diversity in observationally constrained biogenic flux models. In its current configuration, the single biogenic flux model precludes a comprehensive multi-seasonal and annual disentangling of contributions to CO₂; particularly in our annual scale analysis, we are ascribing more uncertainty to the anthropogenic inventories over the biogenic contributions. Absent data from a dense network of ecosystem flux and atmospheric measurements, there will constantly be a tradeoff between drawing conclusions using low-temporal-resolution flask measurements from a few sites and continuous data from a single location.

In situ CO₂ observations interpreted within a high-resolution model framework such as that described in this study provide a powerful constraint to test and correct spatially explicit inventories. The observation station available for the 2005–2009 period was strategically located to provide information on one of the highest CO₂-emitting regions of China. Within the limitations described above, the observations provide strong evidence supporting the use of China-specific methods, such as those employed in ZHAO, for China's CO₂ emissions inventory derivation. In future, access to a spatially dense network of measurements will allow for a sophisticated error analysis that can more readily assess uncertainty in key model components such as transport, flux fields, and background concentrations. Along with the results presented here, previous studies (e.g., Turnbull et al., 2011) provide key information that is necessary to guide and motivate more extensive future measurement and emissions evaluation efforts. Such future efforts will benefit substantially from incorporating newly available information from

column-average CO₂ concentrations acquired by orbiting instruments or ground-based spectrometers to increase observational coverage. A number of existing (OCO-2, OCO-3) and planned satellite missions will significantly reduce the observational gap in China, though surface observations provide additional constraints and a link to absolute calibration scales. A denser network of CO₂ measurement stations in China is required as a component for effective monitoring, reporting, and verification of regional and national inventories. The results of this research present a necessary baseline for a key CO₂-emitting region of China. Our results have broad implications for designing future analyses as more observations of China's CO₂ continue to become available, particularly in the era of increased CO₂ satellite coverage. However, as the quality of satellite retrievals can be compromised by factors such as aerosol loading, surface observations continue to be crucial for the region both in their own right and as a key component of cross-platform evaluations.

Code and data availability. Code and data are available through the Harvard Dataverse at <https://doi.org/10.7910/DVN/OJES00> (Dayalu et al., 2018b). The code and data Supplement includes observational and modeled CO₂ time series, WRF and STILT parameter files, and STILT footprint files.

Supplement. The supplement related to this article is available online at: <https://doi.org/10.5194/acp-20-3569-2020-supplement>.

Author contributions. AD, JWM, and SCW designed the research. AD performed the research with guidance from all co-authors. YW and JWM monitored, maintained, and provided access to the Miyun hourly observational dataset. YZ provided the China-specific anthropogenic inventory. WRF-STILT simulations were performed by AD with assistance from TN. AD constructed the vegetation CO₂ inventory. AD and JWM wrote the paper with contributions from all other co-authors.

Competing interests. The authors declare that they have no conflict of interest.

Acknowledgements. We thank Zhiming Kuang for providing computational resources. We also thank Jenna Samra, Maryann Sargent, and Victoria Liublinska for helpful discussion.

Financial support. This research has been supported by the Harvard-China Project and the Harvard Global Institute.

Review statement. This paper was edited by Christoph Gerbig and reviewed by two anonymous referees.

References

- Andres, R. J., Boden, T. A., and Marland, G.: Annual Fossil-Fuel CO₂ Emissions: Mass of Emissions Gridded by One Degree Latitude by One Degree Longitude v2016. Carbon Dioxide Information Analysis Center, Oak Ridge National Laboratory, US Department of Energy, Oak Ridge, Tenn., USA, <https://doi.org/10.3334/CDIAC/ffe.ndp058.2016>, 2016a.
- Andres, R. J., Boden, T. A., and Higdson, D. M.: Gridded uncertainty in fossil fuel carbon dioxide emission maps, a CDIAC example, *Atmos. Chem. Phys.*, 16, 14979–14995, <https://doi.org/10.5194/acp-16-14979-2016>, 2016b.
- Boden, T. A., Marland, G., and Andres, R. J.: Global, Regional, and National Fossil-Fuel CO₂ Emissions. Carbon Dioxide Information Analysis Center, Oak Ridge National Laboratory, US Department of Energy, Oak Ridge, Tenn., USA, https://doi.org/10.3334/CDIAC/00001_V2016, 2016.
- Brown, D., Brownrigg, R., Haley, M., and Huang, W.: The NCAR Command Language (NCL) v6.0.0, UCAR/NCAR Computational and Information Systems Laboratory, Boulder, CO, <https://doi.org/10.5065/D6WD3XH5>, 2012.
- Dayalu, A.: Exploring the Wide Net of Human Energy Systems: From Carbon Dioxide Emissions in China to Hydraulic Fracturing Chemicals Usage in the United States, PhD thesis, Harvard University, Cambridge, MA, 2017.
- Dayalu, A., Munger, J. W., Wofsy, S. C., Wang, Y., Nehrkorn, T., Zhao, Y., McElroy, M. B., Nielsen, C. P., and Luus, K.: Assessing biotic contributions to CO₂ fluxes in northern China using the Vegetation, Photosynthesis and Respiration Model (VPRM-CHINA) and observations from 2005 to 2009, *Biogeosciences*, 15, 6713–6729, <https://doi.org/10.5194/bg-15-6713-2018>, 2018a.
- Dayalu, A., Munger, J. W., Wang, Y., Wofsy, S. C., Zhao, Y., Nehrkorn, T., Nielsen, C., McElroy, M. B., and Chang, R.: Replication Data for: Evaluating China's anthropogenic CO₂ emissions inventories: a northern China case-study using continuous surface observations from 2005–2009, <https://doi.org/10.7910/DVN/OJES00>, 2018b.
- European Commission, Joint Research Centre (JRC)/Netherlands Environmental Assessment Agency (PBL): Emission Database for Global Atmospheric Research (EDGAR), release EDGARv4.2 FT2010, available at: <http://edgar.jrc.ec.europa.eu> (last access: 13 March 2017), 2013.
- Guan, D., Liu, Z., Geng, Y., Lindner, S., and Hubacek, K.: The gigatonne gap in China's carbon dioxide inventories, *Nat. Clim. Change*, 2, 672–675, <https://doi.org/10.1038/nclimate1560>, 2012.
- Guan, D., Klasen, S., Hubacek, K., Feng, K., Liu, Z., He, K., Geng, Y., and Zhang Q.: Determinants of stagnating carbon intensity in China, *Nat. Clim. Change*, 4, 1017–1023, <https://doi.org/10.1038/nclimate2388>, 2014.
- Jiang, F., Chen, J., Zhou, L., Ju, W., Zhang, H., Machida, T., Ciais, P., Peters, W., Wang, H., Chen, B., Liu, L., Zhang, C., Matsueda, H., and Sawa, Y.: A comprehensive estimate of recent carbon sinks in China using both top-down and bottom-up approaches, *Sci. Rep.-UK*, 6, 22130, <https://doi.org/10.1038/srep22130>, 2016.
- Karion, A., Sweeney, C., Miller, J. B., Andrews, A. E., Commane, R., Dinardo, S., Henderson, J. M., Lindaas, J., Lin, J. C., Luus, K. A., Newberger, T., Tans, P., Wofsy, S. C., Wolter, S.,

- and Miller, C. E.: Investigating Alaskan methane and carbon dioxide fluxes using measurements from the CARVE tower, *Atmos. Chem. Phys.*, 16, 5383–5398, <https://doi.org/10.5194/acp-16-5383-2016>, 2016.
- Kort, E. A., Angevine, W. M., Duren, R., and Miller, C. E.: Surface observations for monitoring urban fossil fuel CO₂ emissions: Minimum site location requirements for the Los Angeles megacity, *J. Geophys. Res.-Atmos.*, 118, 1577–1584, <https://doi.org/10.1002/jgrd.50135>, 2013.
- Le Quééré, C., Andrew, R. M., Canadell, J. G., Sitch, S., Korsbakken, J. I., Peters, G. P., Manning, A. C., Boden, T. A., Tans, P. P., Houghton, R. A., Keeling, R. F., Alin, S., Andrews, O. D., Anthoni, P., Barbero, L., Bopp, L., Chevallier, F., Chini, L. P., Ciais, P., Currie, K., Delire, C., Doney, S. C., Friedlingstein, P., Gkritzalis, T., Harris, I., Hauck, J., Haverd, V., Hoppema, M., Klein Goldewijk, K., Jain, A. K., Kato, E., Körtzinger, A., Landschützer, P., Lefèvre, N., Lenton, A., Lienert, S., Lombardozi, D., Melton, J. R., Metzl, N., Millero, F., Monteiro, P. M. S., Munro, D. R., Nabel, J. E. M. S., Nakaoka, S., O'Brien, K., Olsen, A., Omar, A. M., Ono, T., Pierrot, D., Poulter, B., Rödenbeck, C., Salisbury, J., Schuster, U., Schwinger, J., Séférian, R., Skjelvan, I., Stocker, B. D., Sutton, A. J., Takahashi, T., Tian, H., Tilbrook, B., van der Laan-Luijkx, I. T., van der Werf, G. R., Viovy, N., Walker, A. P., Wiltshire, A. J., and Zaehle, S.: Global Carbon Budget 2016, *Earth Syst. Sci. Data*, 8, 605–649, <https://doi.org/10.5194/essd-8-605-2016>, 2016.
- Lin, J. C., Gerbig, C., Wofsy, S. C., Andrews, A. E., Daube, B. C., Davis, K. J., and Grainger, C. A.: A near-field tool for simulating the upstream influence of atmospheric observations: The Stochastic Time-Inverted Lagrangian Transport (STILT) model, *J. Geophys. Res.-Atmos.*, 108, 4493, <https://doi.org/10.1029/2002JD003161>, 2003.
- Liu, Z., Guan, D., Wei, W., Davis, S. J., Ciais, P., Bai, J., Peng, S., Zhang, Q., Hubacek, K., Marland, G., Andres, R. J., Crawford-Brown, D., Lin, J., Zhao, H., Hong, C., Boden, T. A., Feng, K., Peters, G. P., Xi, F., Liu, J., Li, Y., Zhao, Y., Zeng, N., and He, K.: Reduced carbon emission estimates from fossil fuel combustion and cement production in China, *Nature*, 524, 335–338, 2015.
- Mahadevan, P., Wofsy, S. C., Matross, D. M., Xiao, X., Dunn, A. L., Lin, J. C., Gerbig, C., Munger, J. W., Chow, V. Y., and Gottlieb, E. W.: A satellite-based biosphere parameterization for net ecosystem CO₂ exchange: Vegetation Photosynthesis and Respiration Model (VPRM), *Global Biogeochem. Cy.*, 22, GB2005, <https://doi.org/10.1029/2006GB002735>, 2008.
- Matross, D. M., Andrews, A., Pathmathevan, M., Gerbig, C., Lin, J. C., Wofsy, S. C., Daube, B. C., Gottlieb, E. W., Chow, V. Y., Lee, J. T., Zhao, C. L., Bakwin, P. S., Munger, J. W., and Hollinger, D. Y.: Estimating regional carbon exchange in New England and Quebec by combining atmospheric, ground-based and satellite data, *Tellus B*, 58, 344–358, 2006.
- McKain, K., Wofsy, S. C., Nehr Korn, T., Eluszkiewicz, Ehleringer, J. R., and Stephens, B. B.: Assessment of ground-based atmospheric observations for verification of greenhouse gas emissions from an urban region, *P. Natl. Acad. Sci. USA*, 109, 8423–8428, 2012.
- McKain, K., Down, A., Raciti, S. M., Budney, J., Hutyra, L. R., Floerchinger, C., Herndon, S. C., Nehr Korn, T., Zahniser, M. S., and Jackson, R. B.: Methane emissions from natural gas infrastructure and use in the urban region of Boston, Massachusetts, *P. Natl. Acad. Sci. USA*, 112, 1941–1946, 2015.
- Miller, S. M., Kort, E. A., Hirsch, A. I., Dlugokencky, E. J., Andrews, A. E., Xu, X., Tian, H., Nehr Korn, T., Eluszkiewicz, J., Michalak, A. M., and Wofsy, S. C.: Regional sources of nitrous oxide over the United States: Seasonal variation and spatial distribution, *J. Geophys. Res.*, 117, D06310, <https://doi.org/10.1029/2011JD016951>, 2012.
- Nassar, R., Napier-Linton, L., Gurney, K. R., Andres, R. J., Oda, T., Vogel, F. R., and Deng, F.: Improving the temporal and spatial distribution of CO₂ emissions from global fossil fuel emission data sets, *J. Geophys. Res.-Atmos.*, 118, 917–933, <https://doi.org/10.1029/2012JD018196>, 2013.
- NCEP National Centers for Environmental Prediction/National Weather Service/NOAA/US Department of Commerce: NCEP FNL Operational Model Global Tropospheric Analyses, continuing from July 1999, <https://doi.org/10.5065/D6M043C6>, Research Data Archive at the National Center for Atmospheric Research, Computational and Information Systems Laboratory, Boulder, Co., updated daily, 2000.
- NDRC National Development Reform Commission: Enhanced Actions on Climate Change: China's Intended Nationally Determined Contributions, Beijing, China, available at: <https://www4.unfccc.int/sites/ndcstaging/PublishedDocuments/China%20First/China%27s%20First%20NDC%20Submission.pdf> (last access: 20 March 2020), 2015.
- Nehr Korn, T., Eluszkiewicz, J., Wofsy, S. C., Lin, J., Gerbig, C., Longo, M., and Freitas, S.: Coupled weather research and forecasting–stochastic time-inverted lagrangian transport (WRF–STILT) model, *Meteorol. Atmos. Phys.*, 107, 51–64, <https://doi.org/10.1007/s00703-010-0068-x>, 2010.
- Nielsen, C. and Ho, M.: Clearer Skies Over China: Reconciling Air Quality, Climate, and Economic Goals, MIT Press, ISBN 9780262019880, Cambridge, Mass., USA, <https://doi.org/10.7551/mitpress/9780262019880.001.0001>, 2013.
- Niu, Z., Zhou, W., Wu, S., Cheng, P., Lu, X., Xiong, X., Du, H., Fu, Y., and Wang, G.: Atmospheric Fossil Fuel CO₂ Traced by $\Delta^{14}\text{C}$ in Beijing and Xiamen, China: Temporal Variations, Inland/Coastal Differences and Influencing Factors, *Environ. Sci. Technol.*, 50, 5474–5480, <https://doi.org/10.1021/acs.est.5b02591>, 2016.
- Oda, T., Maksyutov, S., and Andres, R. J.: The Open-source Data Inventory for Anthropogenic CO₂, version 2016 (ODIAC2016): a global monthly fossil fuel CO₂ gridded emissions data product for tracer transport simulations and surface flux inversions, *Earth Syst. Sci. Data*, 10, 87–107, <https://doi.org/10.5194/essd-10-87-2018>, 2018.
- Piao, S., Fang, J., Ciais, P., Peylin, P., Huang, Y., Sitch, S., and Wang, T.: The carbon balance of terrestrial ecosystems in China, *Nature*, 458, 1009–1013, 2009.
- Sargent, M., Barrera, Y., Nehr Korn, T., Hutyra, L., Gately, C., Jones, T., McKain, K., Sweeney, C., Hegarty, J., Hardiman, B., Wang, J., and Wofsy, S.: Anthropogenic and biogenic CO₂ fluxes in the Boston urban region, *P. Natl. Acad. Sci. USA*, 115, 7491–7496, <https://doi.org/10.1073/pnas.1803715115>, 2018.
- Shan, Y., Liu, J., Liu, Z., Xu, X., Shao, S., Wang, P., and Guan, D.: New provincial CO₂ emission inventories in China based on apparent energy consumption data

- and updated emission factors, *Appl. Energy*, 184, 742–750, <https://doi.org/10.1016/j.apenergy.2016.03.073>, 2016.
- Turnbull, J. C., Tans, P. P., Lehman, S. J., Baker, D., Chung, Y., Gregg, J. S., Miller, J. B., Southon, J. R., and Zhao, L.: Atmospheric observations of carbon monoxide and fossil fuel CO₂ emissions from East Asia, *J. Geophys. Res.-Atmos.*, 116, D24306, <https://doi.org/10.1029/2011JD016691>, 2011.
- Ummel, K.: CARMA Revisited: An Updated Database of Carbon Dioxide Emissions from Power Plants Worldwide, CGD Working Paper 304, Center for Global Development, Washington, DC, available at: <http://www.cgdev.org/content/publications/detail/1426429> (last access: 20 March 2020), 2012.
- US EIA (US Energy Information Administration): Total Carbon Dioxide Emissions from the Consumption of Energy, available at: <https://www.eia.gov/beta/international/data/browser>, last access: 12 January 2017.
- Wang, R., Tao, S., Ciais, P., Shen, H. Z., Huang, Y., Chen, H., Shen, G. F., Wang, B., Li, W., Zhang, Y. Y., Lu, Y., Zhu, D., Chen, Y. C., Liu, X. P., Wang, W. T., Wang, X. L., Liu, W. X., Li, B. G., and Piao, S. L.: High-resolution mapping of combustion processes and implications for CO₂ emissions, *Atmos. Chem. Phys.*, 13, 5189–5203, <https://doi.org/10.5194/acp-13-5189-2013>, 2013.
- Wang, X., Wang, Y. X., Hao, J. M., Kondo, Y., Irwin, M., Munger, J. W., and Zhao, Y. J.: Top-down estimate of China's black carbon emissions using surface observations: Sensitivity to observation representativeness and transport model error, *J. Geophys. Res.-Atmos.*, 118, 5781–5795, <https://doi.org/10.1002/jgrd.50397>, 2013.
- Wang, Y., Munger, J. W., Xu, S., McElroy, M. B., Hao, J., Nielsen, C. P., and Ma, H.: CO₂ and its correlation with CO at a rural site near Beijing: implications for combustion efficiency in China, *Atmos. Chem. Phys.*, 10, 8881–8897, <https://doi.org/10.5194/acp-10-8881-2010>, 2010.
- Wang, Y., Wang, X., Kondo, Y., Kajino, M., Munger, J. W., and Hao, J.: Black carbon and its correlation with trace gases at a rural site in Beijing: Top-down constraints from ambient measurements on bottom-up emissions, *J. Geophys. Res.-Atmos.*, 116, D24304, <https://doi.org/10.1029/2011jd016575>, 2011.
- World Bank: CO₂ emissions (kg per PPP \$ of GDP), available at: <https://data.worldbank.org/indicator/EN.ATM.CO2E.PP.GD?locations=CN>, last access: 12 May 2017.
- Zhao, Y., Nielsen, C. P., and McElroy, M.: China's CO₂ emissions estimated from the bottom up: Recent trends, spatial distributions, and quantification of uncertainties, *Atmos. Environ.*, 59, 214–223, 2012.
- Zhao, Y., Zhang, J., and Nielsen, C. P.: The effects of recent control policies on trends in emissions of anthropogenic atmospheric pollutants and CO₂ in China, *Atmos. Chem. Phys.*, 13, 487–508, <https://doi.org/10.5194/acp-13-487-2013>, 2013.